Inhibition of OSBP blocks retrograde trafficking by inducing partial Golgi degradation

He, Nianzhe; Depta, Laura; Rossetti, Cecilia; Caramelle, Lucie; Cigler, Marko; Bryce-Rogers, Hogan P; Michon, Marine; Rafn Dan, Oliver; Hoock, Joseph; Barbier, Julien; Gillet, Daniel; Forrester, Alison; Winter, Georg E; Laraia, Luca

Published in:
Nature Chemical Biology

DOI:
10.1038/s41589-024-01653-x

Publication date:
2024

Document Version
Publisher's PDF, also known as Version of record

Link to publication

Citation for pulished version (HARVARD):
He, N, Depta, L, Rossetti, C, Caramelle, L, Cigler, M, Bryce-Rogers, HP, Michon, M, Rafn Dan, O, Hoock, J, Barbier, J, Gillet, D, Forrester, A, Winter, GE & Laraia, L 2024, 'Inhibition of OSBP blocks retrograde trafficking by inducing partial Golgi degradation', *Nature Chemical Biology*, vol. 21, no. 2, 152, pp. 203-214. https://doi.org/10.1038/s41589-024-01653-x

nature chemical biology

Article

https://doi.org/10.1038/s41589-024-01653-x

Inhibition of OSBP blocks retrograde trafficking by inducing partial Golgi degradation

Received: 5 April 2023

Accepted: 16 May 2024

Nianzhe He[1], **Laura Depta**[1,5], **Cecilia Rossetti**[1,5], **Lucie Caramelle**[2], **Marko Cigler**[3], **Hogan P. Bryce-Rogers**[1], **Marine Michon**[4], **Oliver Rafn Dan**[1], **Joseph Hoock**[1], **Julien Barbier**[4], **Daniel Gillet**[4], **Alison Forrester**[2], **Georg E. Winter**[3] & **Luca Laraia**[1] ✉

Sterol-binding proteins are important regulators of lipid homeostasis and membrane integrity; however, the discovery of selective modulators can be challenging due to structural similarities in the sterol-binding domains. We report the discovery of potent and selective inhibitors of oxysterol-binding protein (OSBP), which we term oxybipins. Sterol-containing chemical chimeras aimed at identifying new sterol-binding proteins by targeted degradation, led to a significant reduction in levels of Golgi-associated proteins. The degradation occurred in lysosomes, concomitant with changes in protein glycosylation, indicating that the degradation of Golgi proteins was a downstream effect. By establishing a sterol transport protein biophysical assay panel, we discovered that the oxybipins potently inhibited OSBP, resulting in blockage of retrograde trafficking and attenuating Shiga toxin toxicity. As the oxybipins do not target other sterol transporters and only stabilized OSBP in intact cells, we advocate their use as tools to study OSBP function and therapeutic relevance.

Lipid homeostasis can be regulated by global and local cholesterol levels, as well as by the levels of its metabolites, including oxysterols[1]. As such, discovering (oxy)sterol interacting proteins and tool compounds to modulate them may reveal regulatory mechanisms and drug targets. Identification of sterol-binding proteins has been carried out using affinity-based proteomic profiling with cholesterol-derived photoactivatable probes identifying more than 200 putative cholesterol interacting proteins[2], while a 20-(*S*)-hydroxycholesterol-derived probe identified the sigma-2 receptor as its primary target[3]. We recently developed a thermal proteome profiling-based approach to identify oxysterol target proteins[4], however, the large number of putative targets made validation efforts challenging.

We reasoned that target identification of (oxy)sterols could be achieved using an approach inspired by targeted protein degradation[5]. Generating proteolysis targeting chimeras (PROTACs) by linking sterols to E3 ligase ligands via different linkers, could lead to the proteasomal degradation of their targets, which could be retrospectively identified using mass spectrometry-based proteomics. While the requirements for ternary complex formation may reduce the number of potentially identifiable targets, we reasoned that this may be an advantage given the relatively promiscuous nature of sterols. Furthermore, a successful sterol-based PROTAC could serve as a tool to study its identified target(s), particularly if selective in its degradation profile.

An important target class for sterols and sterol-based ligands are intracellular sterol transport proteins (STPs). STPs bind and transport

---

[1]Department of Chemistry, Technical University of Denmark, Lyngby, Denmark. [2]Unit of Research of Biochemistry and Cell Biology (URBC), Namur Research Institute for Life Sciences (NARILIS), Université de Namur ASBL, Namur, Belgium. [3]CeMM Research Center for Molecular Medicine of the Austrian Academy of Sciences, Vienna, Austria. [4]Université Paris-Saclay, CEA, INRAE, Département Médicaments et Technologies pour la Santé (DMTS), SIMoS, Gif-sur-Yvette, France. [5]These authors contributed equally: Laura Depta, Cecilia Rossetti. ✉e-mail: luclar@kemi.dtu.dk

sterols, sharing high structural similarities in their sterol-binding domains. They have distinct tissue distributions, intracellular localizations and functions[6]. Additionally, they mediate organelle contacts and lipid metabolism[7]. They have been associated with several diseases including different cancer types, lipid storage disorders and atherosclerosis. The three main families of STPs are oxysterol-binding protein (OSBP)-related proteins (ORPs), the Steroidogenic Acute Regulatory Protein-related Lipid Transfer Domain (STARD) family and the ASTER-domain containing family.

The ORP family contains 12 members, spliced into 16 different isoforms, harboring the oxysterol-binding-protein-related domain (ORD), responsible for lipid binding[8]. OSBP, the prototypic member of this family, binds cholesterol, 25-hydroxycholesterol and PI4P competitively[9]. OSBP localizes to membrane contact sites between the endoplasmic reticulum and other organelles, including the *trans*-Golgi network (TGN), endosomes and lysosomes. OSBP is also a promising drug target. TTP-8307, a known enterovirus replication inhibitor, exerts its antiviral function by targeting OSBP[10] and ORPphilins, a series of natural product OSBP inhibitors, inhibit the growth of p21 deficient cancer cells[11].

Herein we describe the preparation of sterol-based chemical chimeras and their degradation profiles. Substantial degradation of Golgi-associated proteins was observed, with Golgi integral membrane protein 4 (GPP130 or GOLIM4) emerging as the primary target. Target engagement experiments and analysis of the degradation mechanism revealed that the compounds do not act as PROTACs, or directly target GPP130. They induce a more general lysosomal, rather than proteasomal, degradation of several Golgi proteins. By developing an assay panel for profiling activity against STPs, the compounds were ultimately found to potently and selectively target OSBP, leading to inhibition of retrograde trafficking and a reduction in Shiga toxin toxicity.

Results

Degradation profiles of cholesterol-bearing degraders

We aimed to design bifunctional cholesterol (Chol)-bearing degraders (bichols **1**–**4**), by connecting a sterol scaffold with pomalidomide, a commonly used ligand to recruit the E3 Cullin Ring Ubiquitin Ligase cereblon (CRBN) (Fig. 1a, see Extended Data Fig. 1 for synthesis). To exclude proteins affected by the sterol scaffold in absence of the linker and E3 ligase recruiter, the *N*-methylated analog, *N*-methyl cholenamide (**5**), was designed as a negative control. To investigate the proteins affected by **1**–**5** in an unbiased way, we used tandem mass tag (TMT)-based proteomics. HeLa cells were treated with 100 nM and 1 µM **1**–**4** and 1 µM **5** for 18 hours to guarantee a pronounced and sustained degradation of potential targets.

In total, we identified 4,064 proteins by expression proteomics, and 2,454 proteins identified in all replicates were used for further analysis. With a threshold of fold change (FC) > 2 or < 0.5, and $P < 0.05$, no protein was significantly affected by the treatment of 100 nM **1**–**4** or 1 µM **5** (Supplementary Dataset 1). However, the abundance of 21 proteins was significantly altered on treatment with 1 µM **1**–**4** (Fig. 1b), with 14 proteins being degraded and seven being upregulated. Among these, five proteins (GPP130, TM9SF3, TM9SF4, QSOX2 and CD63) have previously been identified as cholesterol interacting proteins by photo-affinity cholesterol probes[2]. Upregulated proteins were initially considered as downstream effects of the degradation of specific proteins and were not further analyzed.

Compound **1**, the only compound containing an alkyl linker, degraded the most proteins (12) while those containing polyethylene glycol linkers (**2**–**4**), degraded ≤6 proteins (Fig. 1c). However, the proteins degraded by **1**–**4** shared similarities: all led to the reduction of GLG1, PI4K2 and GPP130, which are all Golgi proteins. For further validation, we chose GPP130, which was most significantly degraded by **1**–**4** and a known target of cholesterol. GPP130 is a Golgi-resident glycoprotein involved in retrograde trafficking[12]. Loss of GPP130 has been reported to protect from Shiga toxin toxicity, making its degradation by small molecules therapeutically relevant[13].

GPP130 degradation is mediated by the lysosome

Consistent with the proteomics data, western blotting showed that degradation of GPP130 (>90%) could be observed in HeLa cells treated with 1 µM **1**–**4** (Fig. 2a). Although proteomics did not detect significant GPP130 degradation by **1** at 100 nM ($\log_2$ FC = −0.63, $P = 0.26$), degradation was observed by western blotting. No significant depletion of GPP130 was observed in cells treated with 1 µM **5**, indicating that the sterol scaffold alone appears insufficient to cause GPP130 degradation (Fig. 2a). To assess the activity of **1**–**4** across different cell lines, the human lung cancer cell line, A549, was chosen (Fig. 2b). Compounds **1** and **3** decreased GPP130 levels by >90% at 1 µM, while **2** and **4** were limited to <50%. **3** exhibited the best degradation ability and selectivity toward GPP130 and was therefore selected for further validation.

Compound **3** led to a time-dependent degradation of GPP130 over 48 hours, with maximal degradation at 8 hours (Fig. 2c). Compound **3** also exhibited a concentration-dependent degradation of GPP130 (Fig. 2d) with maximal degradation at 2 µM. To explore whether CRBN was required for GPP130 degradation, we first replaced pomalidomide with VH032, a recruiter of the E3 ligase von Hippel Lindau[14]. GPP130 was still degraded, suggesting that degradation of GPP130 was independent of the choice of E3 ligand (Extended Data Fig. 2a,b). Additionally, **6** was synthesized by replacing pomalidomide with *N*-methylated pomalidomide, which is known to abrogate binding to CRBN[15] (Fig. 1c). Compound **6** still led to GPP130 degradation in a concentration-dependent manner, suggesting that CRBN is not involved in GPP130 degradation (Fig. 2e). The degradation of GPP130 by **3** seems independent of the ubiquitin-proteasome system, as HeLa cells treated with the proteasome inhibitor MG132 in conjunction with **3** showed even lower GPP130 levels than when treated with **3** alone (Fig. 2f).

The treatment of MG132 alone led to a pronounced decrease in GPP130 levels. As long-term proteasome inhibition stimulates lysosomal degradation[16], we investigated whether **3** induced lysosomal degradation of GPP130. Cells were treated with the autophagosome-lysosome fusion inhibitor chloroquine, which elevates lysosomal pH by accumulating within lysosomes, or with the v-ATPase inhibitor bafilomycin A1, which inhibits lysosomal acidification by preventing the transfer of protons into lysosomes[17]. The levels of GPP130 were not affected by the treatment of chloroquine alone, while cotreatment with chloroquine and **3** rescued the degradation of GPP130, strongly suggesting that it is lysosome-mediated (Fig. 2f). The cotreatment with bafilomycin A1 and **3** did not lead to GPP130 degradation, while bafilomycin A1 alone did. GPP130 reversibly redistributes to the endosome on pH disruption caused by chloroquine and bafilomycin A1 (refs. 18,19). However, the mechanism by which **3** rescues the degradation of GPP130 induced by bafilomycin A1 remains unclear. We speculate that prolonged inhibition of lysosomal activity may redirect protein degradation to the proteasome when the lysosome is strongly deacidified, while not if the fusion of lysosomes and autophagosomes is impaired[20]. GPP130 degradation by **3** could be partially rescued by inhibitors of specific lysosomal proteases (Extended Data Fig. 2c), where the incomplete rescue can be attributed to the fact that not all lysosomal proteases are inhibited. Additionally, to investigate whether autophagy is involved in GPP130 degradation, HeLa cells were treated with SAR405, an inhibitor of VPS34, which blocks autophagosome biogenesis[21]. SAR405 did not block the degradation of GPP130 induced by **3**, indicating that early autophagy is not involved (Fig. 2f).

A sterol core with a linker triggers GPP130 degradation

As the degradation of GPP130 by **3** does not rely on an E3 ligase or the proteasome, we assumed that the pomalidomide part may not be required. Therefore, we attempted to optimize **3** into smaller GPP130 degraders. The fact that **3** successfully degrades GPP130, but **5** does

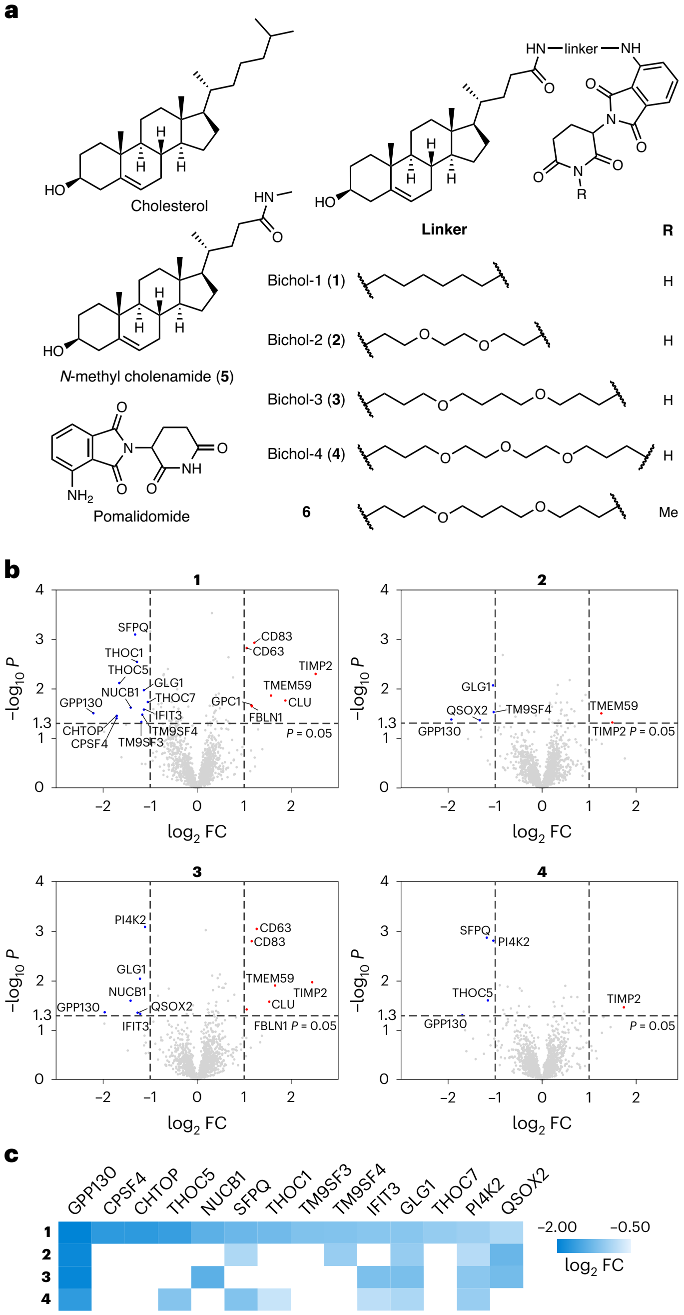

Fig. 1 | Structures and expression proteomics profiles of Chol-based degraders. a, Structures of cholesterol, pomalidomide, bifunctional cholesterols (bichols **1**–**4**), *N*-methyl cholenamide (**5**) and *N*-methylated pomalidomide-bearing degrader, **6**. **b**, Degradation profiles of **1**–**4** at 1 μM in HeLa cells treated for 18 h. The downregulated proteins (blue dots) and upregulated proteins (red dots) were plotted as $\log_2$ FC (compound or DMSO treated) versus $-\log_{10} P$. P values were determined by a Student's two-tailed t-test assuming equal variances from the data of three replicates. The dashed horizontal line marks the significance threshold of $P = 0.05$, and dashed vertical lines represent the threshold of an absolute $\log_2$ FC of 1. **c**, Heatmaps of degraded proteins under the treatment of 1 μM **1**–**4**. See Supplementary Dataset 1 for complete proteomics data.

not, suggests that the linker still plays a role in GPP130 degradation. Therefore, we replaced pomalidomide with a -Boc group, to obtain **7**, and with adamantane, a representative moiety used in hydrophobic tagging strategies (**8**, Fig. 3a)[22]. Both **7** and **8** induced GPP130 degradation in a dose-dependent manner, which confirmed that a sterol core connected to a polyethylene glycol linker is sufficient to trigger GPP130 degradation, irrespective of which moiety was connected at the terminus (Fig. 3a, see Extended Data Fig. 3 for synthesis).

To study whether **3** interacts with GPP130 directly, a cellular thermal shift assay (CETSA) was carried out. **3** only exhibited a weak destabilization effect on GPP130 in cell lysates (Fig. 3b) and intact cells (Extended Data Fig. 4a). Additionally, isothermal dose–response fingerprinting (ITDRF) at 54.3 or 63.4 °C, where the largest differences between control and **3** treated samples were observed, showed that **3** failed to destabilize GPP130 in a dose-dependent manner (Extended Data Fig. 4b). It is therefore likely that the degradation of GPP130 induced by **3** is a secondary effect. This was further supported by the fact that **3** also caused the degradation of QSOX2, another Golgi protein, in a dose- and lysosome-dependent manner (Fig. 3c), similar to **7** and **8** (Fig. 3d). Taken together, we postulated that the observed GPP130 or QSOX2 degradation is not due to direct binding of **3** but a downstream effect stemming from its activity at its primary target.

Compound 3 and its derivatives affect Golgi protein stability

By comparing the bands of GPP130 and QSOX2 by western blotting, it is noticeable that the electrophoretic mobility of GPP130 and QSOX2 are increased under the treatment of **3** and its derivatives (Figs. 2e,f and 3a,c,d). The observed band shift often indicates a change in post-translational modifications of the target protein. As both GPP130 and QSOX2 are highly glycosylated[18,23], we postulated that the shifts are due to incomplete or misglycosylation. To explore whether the *N*-linked glycosylation was affected by **8**, HeLa cells were treated with tunicamycin, a widely used *N*-glycosylation inhibitor. HeLa cell lysates were also treated with PNGase F to cleave most types of *N*-linked oligosaccharide from glycoproteins[23]. Band shifts for QSOX2 can be observed under all tested conditions indicating that the glycosylation state of QSOX2 was affected by tunicamycin and PNGase F (Fig. 3e). Each condition yielded QSOX2 bands at different positions, suggesting that they may affect the extent or the type of glycosylation. However, PNGase F and tunicamycin did not affect *N*-glycosylation of GPP130 under the same conditions, which indicates GPP130 is more likely to be *O*-glycosylated rather than *N*-glycosylated (Extended Data Fig. 4c).

As both GPP130 and QSOX2 are localized at the Golgi[18,23] and most glycosylation reactions occur there, we hypothesized that **3** and its derivatives may affect the stability and glycosylation of other Golgi proteins. Therefore, expression proteomics was conducted to explore the degradation profiles induced by **6**–**8**. In total, up to 8,368 proteins were identified and 6,556 proteins were used for further analysis, where the expression of 37 proteins was significantly altered on compound treatment (Fig. 3f and Supplementary Dataset 1). Compounds **6**–**8** exhibited nearly identical degradation profiles (Fig. 3g). Manganese(II), which is reported to target several Golgi proteins including GPP130 and GLG1 (ref. 24) and leads to GPP130 oligomerization and degradation[13,25,26], exhibited a distinct degradation profile compared to **3** and its derivatives (Fig. 3h). The levels of only three proteins (GPP130, GLG1 and EXTL3) were significantly reduced by both **6**–**8** and Mn^{2+}, while other known Mn^{2+} binding proteins such as aminopeptidase-like 1 and NDRG1 (ref. 27) were down- or upregulated by Mn^{2+}, respectively. As such, it appears that the GPP130 degradation mechanisms of Mn^{2+} and the derivatives of **3** are different. The data provided may enable the discovery of new Mn^{2+}-binding proteins (Supplementary Dataset 1).

The proteins whose levels were reduced by **6**–**8** exhibited striking similarities (Fig. 3i). STRING functional enrichment analysis revealed an enrichment of Golgi proteins (16 out of 23) and glycosyltransferases (six out of 23), which further support the fact that the increased mobility of GPP130 and QSOX2 is due to misglycosylation. In addition, several proteins (11 out of 23) are also found in coat protein complex I (COPI) vesicles[28]. COPI is mainly responsible for trafficking cargoes within the Golgi and retrograde trafficking from the Golgi to endoplasmic reticulum. Therefore, the data also indicate that COPI-mediated retrograde trafficking was affected by **6**–**8**. We hypothesized that these

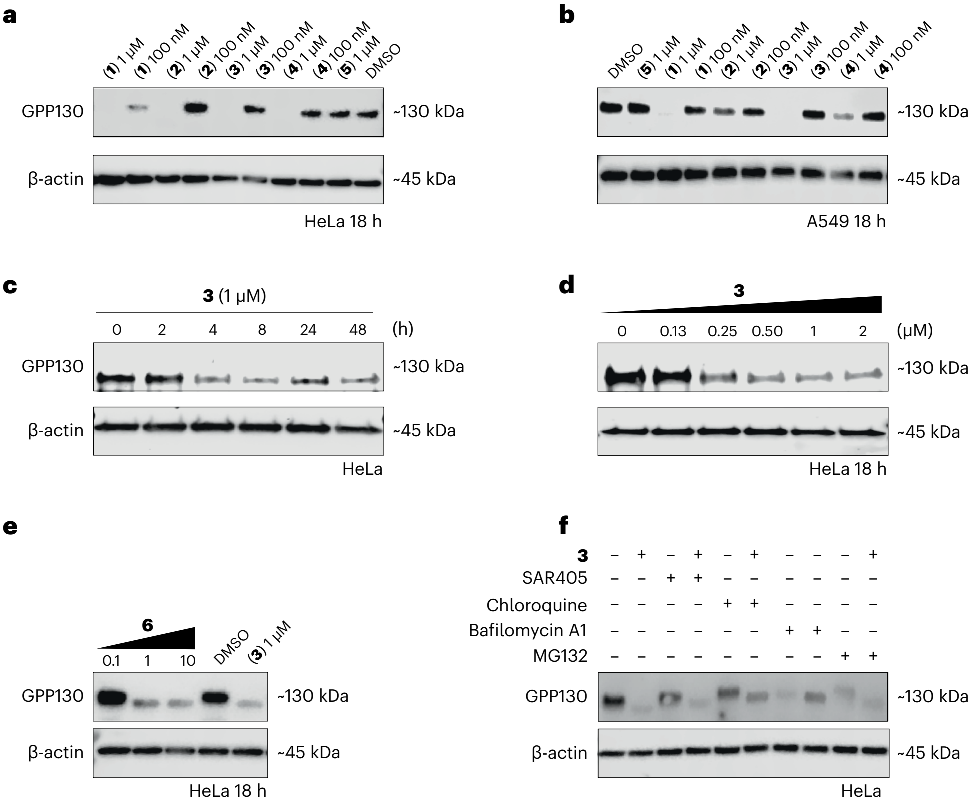

Fig. 2 | Validation of GPP130 degradation by 1–4. a,**b**, Changes in GPP130 levels in response to **1**–**4** in HeLa (**a**) and A549 cell lines (**b**) (18 h, *n* = 2). **c**, Time dependency of GPP130 degradation in HeLa cells by **3** (*n* = 4). **d**, Dose-dependent degradation of GPP130 in HeLa cells by **3** (18 h, *n* = 4). **e**, Degradation of GPP130 in HeLa cells by **6** (18 h, *n* = 2). **f**, Requirement of a functional proteasome or lysosome for the degradation of GPP130 by **3**. HeLa cells were treated with MG132 (10 µM), chloroquine (20 µM), bafilomycin A1 (100 nM) and SAR405 (100 nM) in the absence or presence of **3** (1 µM) for 18 h (*n* = 3). See Supplementary Fig. 1 for quantification.

compounds interact with a Golgi component, affecting normal Golgi functions and leading to degradation of Golgi-resident proteins.

Compound 3 and its derivatives selectively target OSBP

Having ruled out that **3** and its derivatives interact with GPP130, and given that they contain a sterol scaffold, we hypothesized that the observed phenotypes may be due to the binding of STPs. In particular, OSBP localizes to endoplasmic reticulum–Golgi contact sites, cycling cholesterol and PI4P between the endoplasmic reticulum and the Golgi[9]. Additionally, the inhibition or depletion of OSBP has been reported to lead to the reduction of mannosidase II levels and the mislocalization of COPI vesicles[29] as well as Golgi fragmentation and impaired Golgi trafficking[30–32]. Owing to the similarities in the sterol-binding domains of OSBP and other STPs[6,8,33–35], we sought to establish an STP screening panel comprising OSBP, ORP1 and ORP2 as members of the ORP family, STARD1, as a representative member of the STARD family as well as Asters A–C.

To establish a selectivity panel, we developed competitive fluorescence polarization (FP) assays using 22-NBD-cholesterol as a tracer molecule. The ORD of OSBP was expressed harboring a glutathione *S*-transferase (GST) tag to maintain sufficient stability and solubility of the protein. GST alone did not interfere with 22-NBD-cholesterol binding (Fig. 4a). The sterol-binding domains of ORP1, ORP2 and STARD1 were expressed with an N-terminal His$_6$ tag and the ASTER domain of the Aster proteins was expressed with a GST tag, which was later removed via protease cleavage[36,37]. The 22-NBD-cholesterol efficiently binds to all STPs (Fig. 4a) indicating its suitability as a FP assay tracer. The 25-NBD-cholesterol bound ORP1 and ORP2 more tightly and can be used as an alternative (Extended Data Fig. 5a). The calculation of Z′ factors indicated that the competitive FP assay for the STPs is robust and suitable for the evaluation of ligand binding affinity (Extended Data Fig. 5b). We screened **7**, **8** and controls toward OSBP, ORP1, ORP2, STARD1 and the Aster proteins at concentrations of 1 µM (Fig. 4b) and 3 µM (Extended Data Fig. 5c). Compounds **7** and **8** completely inhibited GST-OSBP(ORD) binding to 22-NBD-Chol at 1 µM, similar to the endogenous OSBP ligand 25-OH-cholesterol (25-OHC) and the known inhibitor OSW-1, while not showing any inhibition of the other sterol transporters (Fig. 4b). As such, we renamed them oxybipin-1 (**8**) and -2 (**7**), for oxysterol-binding protein inhibitors. We subsequently screened oxybipin-1, and -2 as well as **5**, 25-OHC and OSW-1 against GST-OSBP(ORD) in a dose-dependent manner (Fig. 4c). Both oxybipin-1 (half-maximum inhibitory concentration (IC$_{50}$) 77 nM) and oxybipin-2 (IC$_{50}$ = 13 nM) were potent inhibitors of the OSBP–22-NBD-Chol interaction. Compound **5** also showed some activity, although to a lower degree. To determine whether the inhibition of OSBP binding to cholesterol derivatives also resulted in the ability to inhibit sterol transport, we developed a Förster resonance energy transfer (FRET)-based assay in liposomes. Donor lipososomes (D) containing the FRET pair 23-BODIPY-cholesterol (BODIPY-Chol) and rhodamine 1,2-dihexadecanoyl-*sn*-glycero-3-phosphoethanolamine (Rh-DHPE) were incubated with unlabeled acceptor (A) liposomes in the presence or absence of OSBP and test compounds. Similar to the positive control OSW-1, both oxybipins were able to completely inhibit the transport of cholesterol in liposomes, as assessed by a lack of reduction in FRET signal (Fig. 4d).

Subsequently, we aimed to determine cellular target engagement of OSBP and related ORPs using a CETSA in a split nanoluciferase (HiBiT-LgBiT) system in KBM7 cells overexpressing HiBiT-tagged OSBP, as well as the closely related ORP4L and ORPs 2 and 9 (Fig. 4e,f and Extended Data Fig. 5d)[38]. Consistent with the biochemical data,

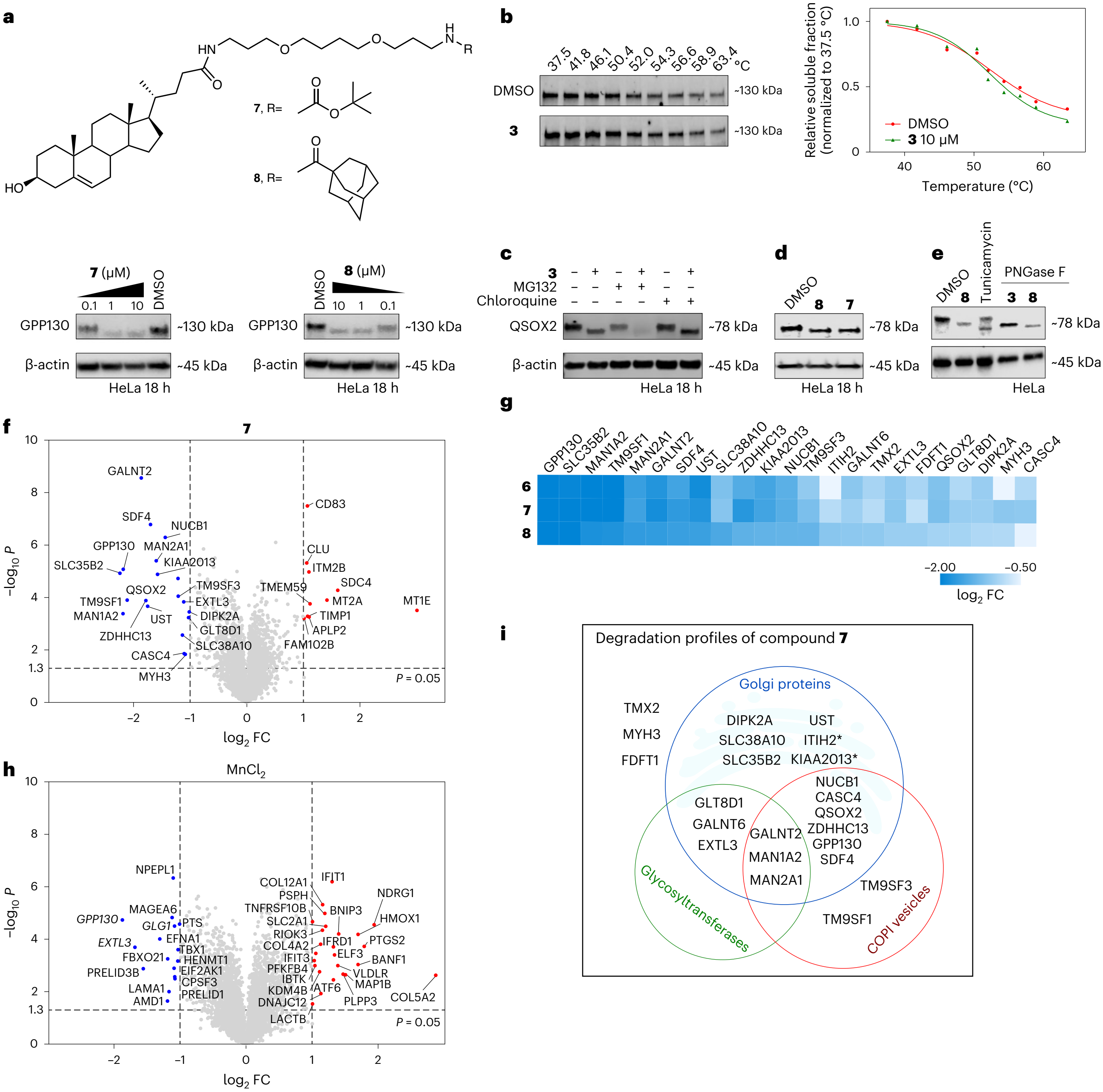

Fig. 3 | Compounds 6–8 significantly degrade Golgi proteins. a, Degradation of GPP130 by **7** and **8**. Top: Chemical structures of **7** and **8**. Bottom: Degradation abilities of **7** and **8** ($n = 2$). **b**, Thermal stability of GPP130 in HeLa cell lysate in response to **3** as assessed by a CETSA ($n = 2$). Left: Representative image. Right: CETSA curve. **c**, Mechanism of QSOX2 degradation by **3**. HeLa cells were treated with MG132 (10 μM), chloroquine (20 μM) in the absence or presence of **3** (1 μM) for 18 h ($n = 2$). **d**, Degradation of QSOX2 by **7** and **8** (1 μM) in HeLa cells after 18 h ($n = 2$). **e**, N-glycosylation of QSOX2 is altered by tunicamycin (5 μg ml^{-1}) for 18 h, PNGase F and **8** ($n = 2$). **f**, Expression proteomics profile of **7** at 1 μM for 18 h in HeLa cells. The downregulated proteins (blue dots) and upregulated proteins (red dots) were plotted as $\log_2$ FC (compound or DMSO treated) versus $-\log_{10} P$. *P* values were determined by a Student's two-tailed *t*-test assuming equal variances from the data of three technical replicates. The dashed horizontal line marks the significance threshold of $P = 0.05$, and dashed vertical lines represent the threshold of an absolute $\log_2$ FC of 1. **g**, Heatmaps of degraded proteins under the treatment of 1 μM **6**–**8**. **h**, Degradation profiles of $MnCl_2$ at 150 μM for 18 h in HeLa cells. The downregulated proteins (blue dots) and upregulated proteins (red dots) were plotted as $\log_2$ FC (compound or DMSO treated) versus $-\log_{10} P$. *P* values were determined by a Student's two-tailed *t*-test assuming equal variances from the data of three technical replicates. Proteins affected by both **3** analogs and $MnCl_2$ are marked in italics. **i**, The degraded proteins can be classified into three groups: Golgi proteins (blue circle GO:0005794; FDR 8.76×10^{-10})—Golgi proteins not enriched by STRING functional analysis are labeled with an asterisk; glycosyltransferases and proteins involved in glycoprotein biosynthetic process (green circle, GO:0009101; FDR 0.0146); and COPI vesicles (red circle). See Supplementary Dataset 1 for the complete proteomics data.

oxybipin-1 and -2 exhibited a substantial stabilizing effect on OSBP with $\Delta T_m > 5$ °C while the less active control **5** only exhibited a weak stabilization of OSBP ($\Delta T_m \approx 1$ °C). Notably, no stabilizing effect of the oxybipins could be observed on other ORPs including the highly structurally related ORP4L (Fig. 4f), as well as ORP2 and -9 (Extended Data Fig. 5d). Selectivity among related STPs is challenging due to the similarity in the sterol-binding domain, however, a recent report highlighted that different oxysterols have differential binding preferences to OSBP and ORP4 based on the site and extent of their oxidation pattern[39]. Our compounds may mimic this effect with the position of the amide and ether heteroatoms on the sterol side chain.

To comprehensively evaluate the selectivity profile of oxybipins across the proteome, two noncovalent pulldown probes, **9** and **10**, were synthesized (Extended Data Fig. 5e and Supplementary Fig. 2). Despite still binding to OSBP in vitro (Extended Data Fig. 5f), these probes failed to enrich OSBP from lysates (Extended Data Fig. 5g), possibly by interacting with the beads directly, preventing the interaction with target proteins. Therefore, an isothermal shift assay (iTSA) with a mass spectrometric readout was conducted.[40] iTSA is based on the principle that small molecule binding can alter the thermostability of its target protein in a dose-dependent way at a single temperature. The ability to discern dose-dependent effects is a critical component of iTSA, as thermal proteome profiling experiments are typically carried out at a single concentration that is much higher than the one used in cellular experiments, leading to false positives. We treated HeLa cells with oxybipin-2 at four concentrations and heated intact cells to 53 °C, which is the average melting temperature (T_m) of the human proteome and thus the most likely to enable the observation of changes to protein stability.[41,42] The changes in protein levels compared to a dimethylsulfoxide (DMSO) control were obtained through quantitative proteomics.

Here, 5,389 proteins were identified and 3,938 were used for further analysis. Of the ORP family, OSBP and ORP9 were identified. OSBP was the only protein that was significantly and dose-dependently stabilized on treatment with increasing concentrations of oxybipin-2 (Fig. 4g,h, Extended Data Fig. 5h and Supplementary Dataset 1). While a few destabilized proteins were identified, only YME1L1 (ATP-dependent zinc metalloprotease) and ABCF2 (ATP-binding cassette subfamily F member 2) exhibited dose-dependent effects at 10 and 3 µM oxybipin-2 (Extended Data Fig. 5d). Notably, no protein other than OSBP was (de)stabilized by 1 µM oxybipin-2 treatment, which indicates excellent selectivity even at the highest concentration used in all subsequent experiments.

OSBP inhibition by a set of structurally unrelated natural products termed the ORPphilins has been shown to produce diverse effects on OSBP and ORP4 protein levels[11], with compounds including OSW-1 leading to the proteasomal degradation of OSBP through an unknown mechanism. OSBP and ORP4S levels were not affected by the treatment of oxybipin-1 and -2, unlike OSW-1 (Fig. 4i). To compare the similarity in phenotypes elicited by OSW-1 and our new OSBP inhibitors, we carried out expression proteomics on cells treated with OSW-1 and **3** (Supplementary DataSet 1 and Extended Data Fig. 6a,b). In total, 6,906 proteins were identified and 5,157 proteins were used for further analysis. Excluding OSBP, OSW-1 and **3** exhibited nearly identical degradation profiles, where downregulated proteins were highly enriched in Golgi proteins and proteins involved in *N*-glycan biosynthesis (Extended Data Fig. 6c), which confirms that the phenotypes induced by oxybipins result from OSBP inhibition. Proteomics further confirmed that OSW-1 significantly degrades OSBP ($\log_2 FC = -0.8$, $P < 0.001$) while **3** did not ($\log_2 FC = 0.2$, $P < 0.05$), suggesting that while the phenotypes they elicit are similar, their mechanisms differ. Similarly to the oxybipins, OSW-1 treatment also led to the significant degradation of GPP130 (Extended Data Fig. 6d).

Benchmarking the oxybipins against known OSBP inhibitors

To benchmark the oxybipins against previously reported OSBP inhibitors we synthesized or acquired T-00127-HEV-2, -3 and -4 (THEVs)[43,44], itraconazole (ITZ)[45] and TTP-8307 (TTP)[10] in addition to the aforementioned OSW-1, and profiled them in our panel of biophysical assays (Extended Data Fig. 7a). At 1 µM, THEV2/3/4 show complete inhibition of OSBP in the FP assay, however, they also displayed potent activity against ORP1 and ORP2, potentially resulting in a weak selectivity profile (Extended Data Fig. 7b). Notably, THEV3/4 were shown to bind OSBP directly, although they were originally developed as ligands for the estrogen-related receptor gamma (ERRγ)[46]. Dose–response measurements confirmed the potent activity of THEV3 and -4 against ORP1 (Extended Data Fig. 7c) and ORP2 (Extended Data Fig. 7d), close to the limit of detection of the assays, while THEV2 had a better selectivity profile. Despite using a protein concentration of 250 nM in the FP assay, dose–response measurements against OSBP revealed IC_{50} values for THEV2 (2 nM), THEV3 (26 nM) and THEV4 (7.5 nM) in the low nanomolar range (Extended Data Fig. 7e). To further investigate this phenomenon, we performed dynamic light scattering (DLS) measurements, which indicated the presence of two different species in all samples. While the size of the first species corresponds to an GST-OSBP(ORD) monomer, the size of the second species corresponds to a trimer (Extended Data Fig. 7f). Formation of larger oligomeric species was observed when GST-OSBP(ORD) was treated with THEV2, which may explain its unexpectedly high potency. ITZ and TTP on the other hand showed very weak inhibition of OSBP ($IC_{50} \geq 10$ µM). Furthermore, they were only weakly able to inhibit OSBP-mediated cholesterol transport in the sterol transfer assay at 10 µM (Extended Data Fig. 7g). This, combined with the extensive off-target activity of ITZ[47] makes them unsuitable tools for the study of OSBP function (see Extended Data Fig. 7h for an overview of the activities of all compounds against all sterol transporters).

To rationalize the structure–activity relationships and relative affinity of the oxybipins and reported OSBP inhibitors, we performed molecular docking with a crystal structure of OSBP (Protein Data Bank (PDB) 7V62, Extended Data Fig. 8)[44]. Oxybipin-2 is predicted to bind with the sterol A-D ring system oriented toward the bottom of the pocket, maintaining key residue interactions suggested for cholesterol (Extended Data Fig. 8a,b). Furthermore, Oxybipin-2 shows a key hydrogen bond with T491 before the exit of the linker from the pocket. This interaction is not predicted for any other class of inhibitors, providing an explanation for the oxybipins' selectivity. In that regard, irrespective of the functionalization at the linker terminus, the cholesterol anchor and other key interactions remain inside the binding domain (Extended Data Fig. 8c,d). The high affinity of THEV2/3/4 can be explained through a combination of hydrophobic interactions and conserved, key hydrogen bonds at the bottom of the pocket, mimicking the cholesterol 3-OH group (Extended Data Fig. 8e–g). As suggested previously[44], THEV2 appears to be oriented with the tetrahydropyran protecting group facing toward the exterior of the binding site.

OSBP inhibitors impair retrograde trafficking

OSBP relocalization and Golgi fragmentation have been detected in response to OSBP inhibition by OSW-1 (ref. 32), OSBP knockdown[31] and OSBP mutations[48]. Thus, we examined whether oxybipins can enhance localization of OSBP to the Golgi, and whether the phenotype differed compared to other ligands[49]. We observed a significantly increased localization of OSBP to the Golgi area as marked by TGN46, a commonly used TGN marker, on treatment with oxybipin-2 at 100 nM and 1 µM after 4 and 8 hours. Other OSBP inhibitors including OSW-1, TPP and ITZ exhibited similar effects, confirming that OSBP inhibition leads to increased localization of OSBP to Golgi (Fig. 5a–c and Extended Data Fig. 9a–d). Oxybipin-2 (1 µM) significantly led to fragmentation of the Golgi at 4 hours, as indicated by an increased number of TGN46 spots. Oxybipin-2 (100 nM) failed to induce significant Golgi fragmentation after 4 hours (Fig. 5b,c) but started to induce Golgi fragmentation after 8 hours (Extended Data Fig. 9b,c). OSW-1 also induced Golgi fragmentation, as previously suggested[32], however, this was less pronounced

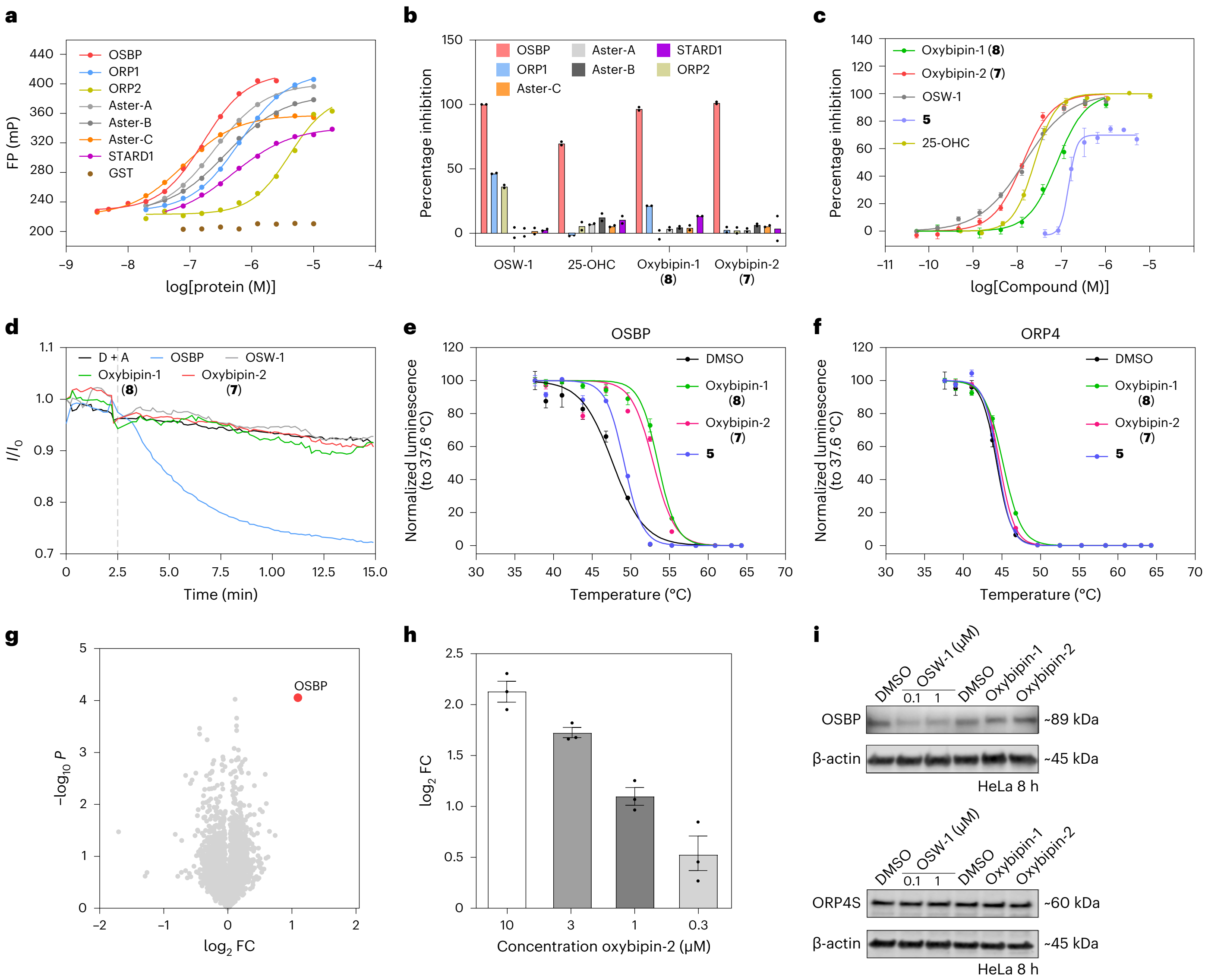

Fig. 4 | Oxybipin-1 and -2 selectively target OSBP. **a**, Binding curve of the FP titration of 22-NBD-cholesterol with STPs and GST. Each data point represents the mean of a representative experiment ($N = 2$), from three independent experiments ($n = 3$). **b**, Screening of **8** (oxybipin-1), **7** (oxybipin-2), OSW-1 and 25-OHC in the STP FP selectivity panel at 1 µM. Each bar represents the mean of a representative experiment ($N = 2$), from three independent experiments ($n = 3$). **c**, Dose-dependent inhibition of GST-OSBP-ORD binding to 22-NBD-Chol as assessed by FP. Data are represented as mean ± s.e.m from three independent experiments ($N = 3$, $n = 3$). **d**, Inhibition of sterol transport by GST-OSBP(ORD) (500 nM) in liposomes using a FRET assay. All compounds were used at 500 nM. One representative experiment was shown from three independent experiments ($n = 3$). D, donor liposomes; A, acceptor liposomes. **e**,**f**, Effect on the stability of OSBP (**e**) and ORP4L (**f**) by oxybipin-1 and -2 in intact KBM7 cells expressing HiBit-tagged fusion proteins. Each data point represents mean ± s.e.m from three technical replicates of a representative experiment ($N = 3$), from three independent experiments ($n = 3$). **g**, Changes in thermal stability of proteins after treatment with oxybipin-2 (1 µM) in HeLa cells at 53 °C; The stabilized protein (red dot) was plotted as $\log_2$ FC (compound or DMSO treated) versus $-\log_{10} P$. P values were determined by a Student's two-tailed t-test assuming equal variances were calculated from the data of three replicates. **h**, Dose-dependent stabilization of OSBP by oxybipin-2 in iTSA experiments. Mean ± s.e.m.; $n = 3$. See Supplementary Dataset 1 for complete proteomics data. **i**, Effect on cellular OSBP and ORP4S levels by 1 µM oxybipin-1 and -2 as well as OSW-1 in HeLa cells after 8 h ($n = 2$, representative experiment shown).

with ITZ and TTP, in line with their reduced in vitro potency (Fig. 5c and Extended Data Fig. 9). To test whether protein trafficking in the cell was perturbed, we used the classical retrograde transport cargo Shiga toxin (STx), to assess whether OSBP inhibition would affect retrograde transport. If the retrograde trafficking of STx is inhibited, it will be transferred from early endosomes to the lysosome for degradation or be directed to recycling endosomes to be expelled from the cell in extracellular vesicles. Notably, OSBP KD has been reported to affect the localization of GS28, a protein involved in Golgi trafficking[29]. In control conditions, most of fluorescently labeled STx B-subunit (STxB) reached the Golgi, colocalizing with the Golgi marker, giantin (Fig. 5d,e). In cells treated with oxybipin-2 (Fig. 5d,e), OSW-1 and ITZ (Extended Data Fig. 9e,f), less STxB colocalized with giantin and instead colocalized with transferrin receptor (TfR), a commonly used early and/or recycling endosomal marker, indicating that STxB remained trapped in early endosomes due to impaired retrograde trafficking[50]. This was not the case for TPP, THEV2/3/4 and the less active control **5**, which behaved similarly to the DMSO control, although it cannot be excluded that these compounds may show activity at higher concentrations than those tested (10 µM).

To further explore whether OSBP inhibition could protect cells against STx toxicity, we compared the protein biosynthesis rate in the presence of STx1 with and without **3** and oxybipin-1 treatment. The protein synthesis rate was measured by the incorporation of radiolabeled

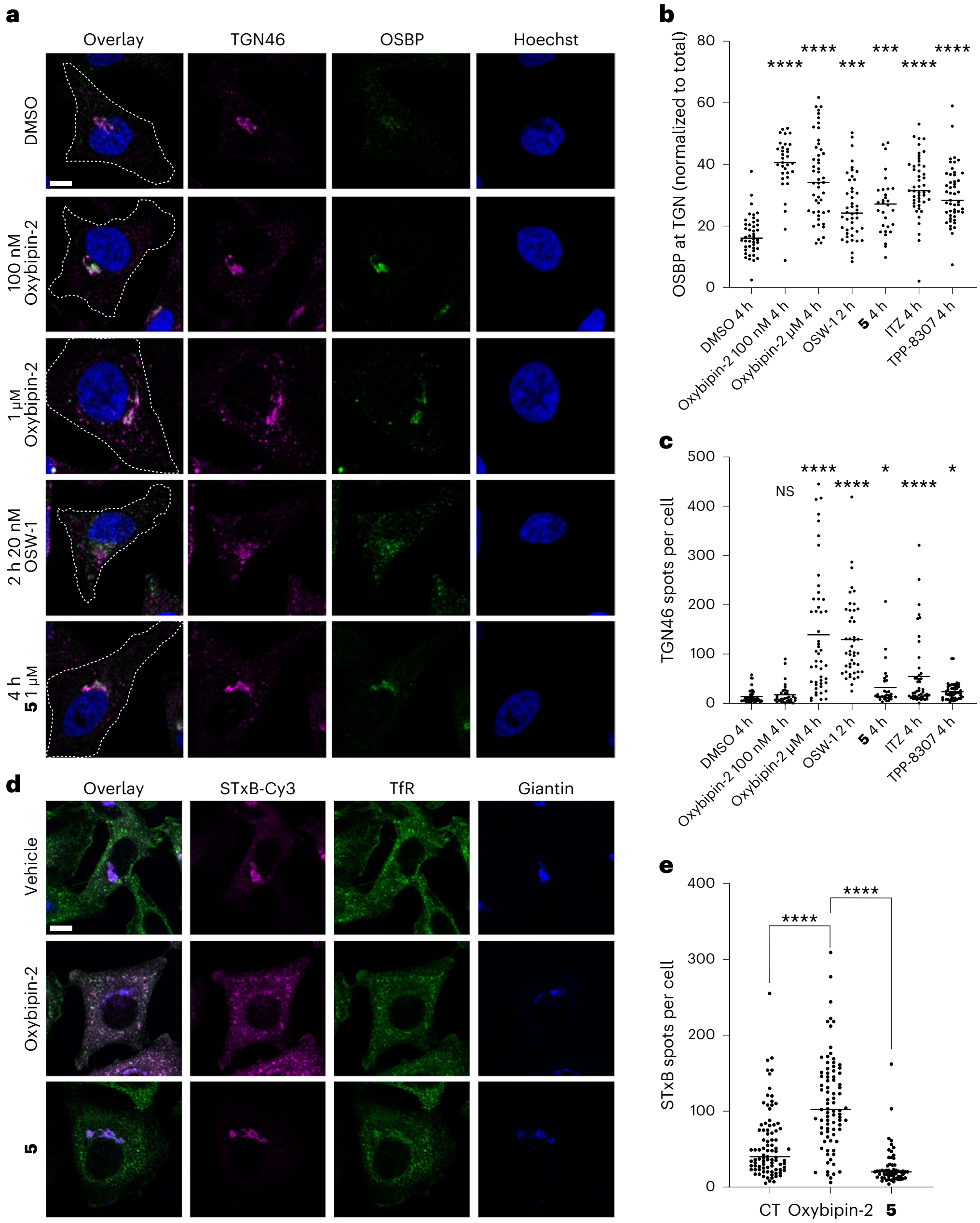

Fig. 5 | OSBP inhibition causes OSBP localization to the Golgi, *trans*-Golgi fragmentation and inhibition of STxB trafficking. a, Scanning confocal microscopy of HeLa cells treated with DMSO, 100 nM or 1 μM oxybipin-2 or 1 μM **5** for 4 h, or 20 nM OSW-1 for 2 h. Cells were immunolabelled with TGN46 (647) and OSBP (488), nuclei labeled with Hoechst. Scale bar, 10 μm; dotted lines indicate cell outline. **b**, Quantification of data shown in **a** and Extended Data Fig. 9a, of OSBP localization to the Golgi, labeled by TGN46. OSBP fluorescence intensity was measured in TGN46 ROI and normalized to total cellular OSBP. OSBP localization: one-way ANOVA was performed ($P < 0.0001$) with Dunnett's multiple comparison test; ***$P = 0.002$ (OSW-1), ***$P = 0.002$ (**5**), ****$P < 0.0001$. **c**, Quantification of data shown in **a** and Extended Data Fig. 9a of TGN46 fragmentation measured by number of spots per cell. Golgi fragmentation: one-way ANOVA was performed on $\log_{10}$ transformed data ($P < 0.0001$) with Dunnett's multiple comparison test; not significant (NS), $P > 0.9999$, *$P = 0.0179$ (**5**), *$P = 0.0106$ (TPP-8307), ****$P < 0.0001$. **b**,**c**, Graphs show one point per cell, shape represents each independent experimental replicate ($n = 3$) for a total of 44 (DMSO), 33 (100 nM oxybipin-2, $n = 2$), 49 (1 μM oxybipin-2), 45 (OSW-1), 30 (**5**, $n = 2$), 47 (ITZ) and 49 (TPP-8307); horizontal line indicates mean. **d**, Scanning confocal images of STxB-Cy3 trafficking in HeLa cells treated for 4 h with DMSO vehicle, 1 μM oxybipin-2 or **5**. Cells were immunolabelled with TfR (488), giantin (647) and nuclei stained with Hoechst. Scale bar, 10 μm. **e**, Quantification of STxB measured by number of spots per cell. Graph shows one point per cell; horizontal line indicates mean. One-way ANOVA was performed ($P < 0.0001$) with Dunnett's multiple comparisons test to compare CT and **5** to oxybipin-2: ****$P < 0.0001$. DMSO control (CT) and oxybipin-2 ($n = 3$) for a total of 89 (DMSO), 83 (oxybipin-2) and 58 (**5**, $n = 1$).

[^{14}C]-leucine into newly synthesized proteins. Oxybipin-1 exhibited a 14-fold protection at 3 μM and **3** exhibited a fivefold protection at 1 μM, while **5** did not exhibit any protection (Fig. 6a). Cell viability measurements showed that **3** and oxybipin-1 do not promote cell death in HeLa cells up to 10 μM after 24 hours with minor effects at 30 μM (Extended Data Fig. 10a).

We subsequently used dose-dependent cell viability experiments to characterize the cellular effects of oxybipin-mediated OSBP inhibition in a panel of leukemia cell lines. These have been recently reported to be sensitive to OSBP inhibition[38]. While oxybipin-2 is toxic to the leukemia cell lines Jurkat (Extended Data Fig. 10b, half-maximum effective concentration (EC_{50}) of 162 nM), MOLM13 (Extended Data Fig. 10c,

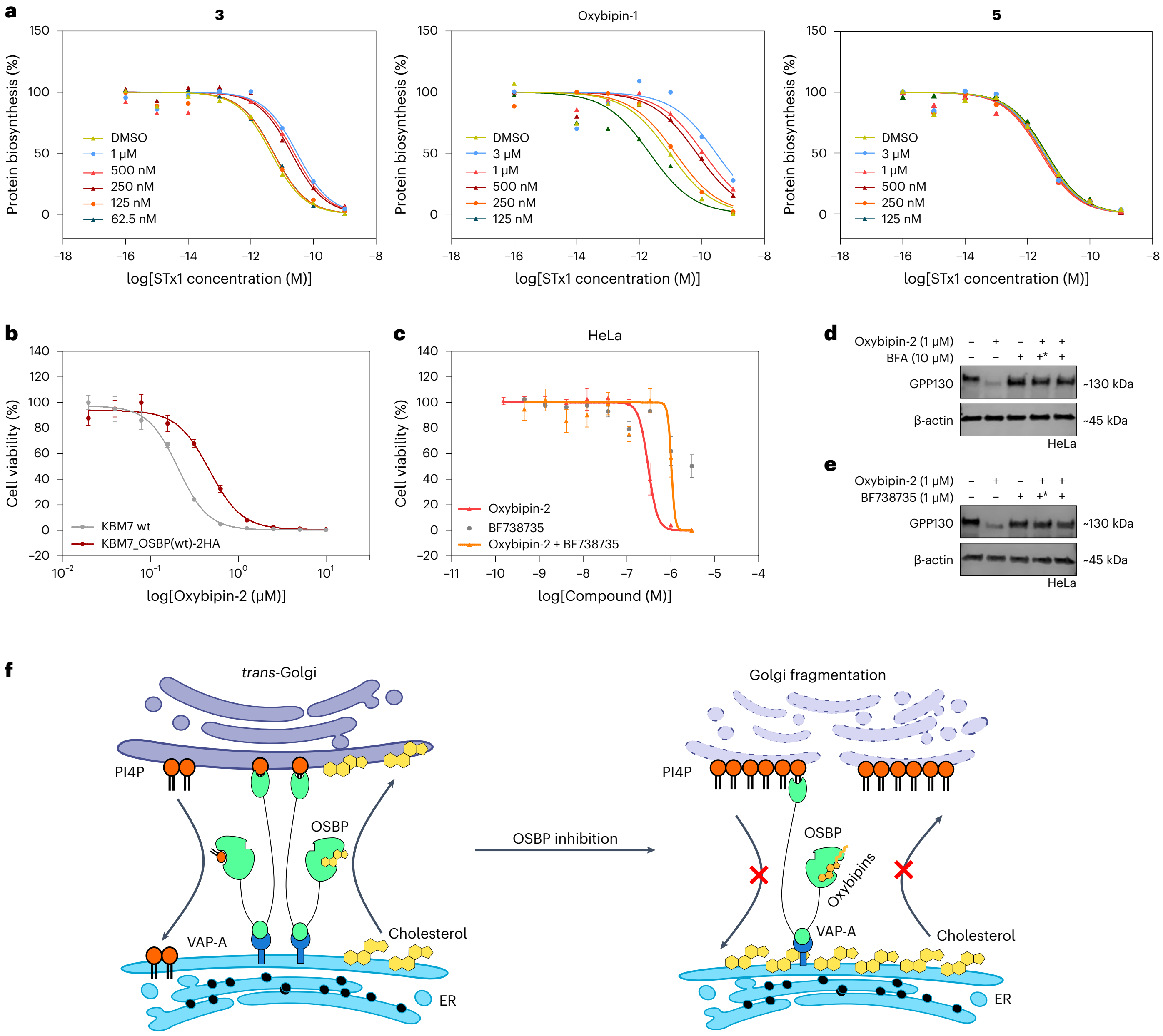

Fig. 6 | Therapeutic potential and mechanism of action of OSBP inhibitors. **a**, Protection conferred by **3** (left), oxybipin-1 (middle) and **5** (right) against STx1 protein biosynthesis inhibition. Each data point represents the mean of a representative experiment (*N* = 2), from three independent experiments (*n* = 3). **b**. Effect of oxybipin-2 on the viability of KBM7 wild-type (WT) cells and KBM7 cells overexpressing OSBP(WT)-2HA. Each data point represents mean ± s.e.m from three technical replicates of a representative experiment (*N* = 3), from three independent experiments (*n* = 3). **c**, Effect of oxybipin-2, PI4K inhibitor BF738735 as well as the cotreatment of oxybipin-2 and BF738735 on HeLa cell viability. Each data point represents mean ± s.e.m from three independent experiments (*n* = 3). **d**, GPP130 degradation rescue by redistribution to the ER. HeLa cells were pretreated (indicated by asterisk) with BFA (10 µM) for 2 h or cotreated in the absence or presence of oxybipin-2 (1 µM) for 18 h (*n* = 2, representative experiment shown). **e**, GPP130 degradation rescue by PI4K inhibition. HeLa cells were pretreated (indicated by asterisk) with BF738735 (10 µM) for 2 h or cotreated in the absence or presence of oxybipin-2 (1 µM) for 18 h (*n* = 2, representative experiment shown). **f**, Model for the mechanism of action of oxybipins. Under normal conditions, the balance between PI4P and cholesterol mediated by OSBP maintains Golgi integrity, morphology and normal function. When the OSBP is inhibited by oxybipins, the exchange between PI4P and cholesterol is blocked, leading to the accumulation of PI4P at *trans*-Golgi. The imbalance between PI4P and cholesterol results in the fragmentation of Golgi and the degradation of Golgi proteins. ER, endoplasmic reticulum.

EC_{50} = 120 nM) and KBM7 (Fig. 6b, EC_{50} = 200 nM), **5** did not affect cell viability (Extended Data Fig. 10b,c). Despite potent activity against OSBP as well as their ability to bind ORP1 and ORP2 in vitro (Extended Data Fig. 5h), THEV2, -3 and -4 showed weak effects on cell viability. This may indicate their instability in a cellular environment, possibly due to the acid-labile THP protecting group (THEV2) and the hydrolyzable acyl hydrazones (THEV3 and -4). To investigate this, the stability of THEV3/4 were tested in DMEM and acidic H_2O (pH 4.5, mimicking lysosomes). The decomposition of both compounds was observed immediately in acidic H_2O and after 24 hours in DMEM (Supplementary Figs. 3 and 4). In addition to leukemia cell lines, we also tested the effect of OSBP inhibition in HeLa cervical cancer cells (Fig. 6c and Extended Data Fig. 10d,e). In line with recent reports for other OSBP inhibitors, these cells were also sensitive to oxybipins at 72 h. The fact that no cytotoxicity was observed in the same cell line at 24 h (Extended Data Fig. 10a), suggests that cells can cope with a fragmented Golgi for short periods. The toxicity of oxybipins (Fig. 6b and Extended Data Fig. 10f) and OSW-1 (Extended Data Fig. 10g) were markedly attenuated in KBM7 cells overexpressing OSBP, confirming this as their relevant biological target. However, this effect was less pronounced for THEV2 and was not observed for THEV3/4, **5** and the negative control Taxol (Extended Data Fig. 10h–l).

To investigate the mechanism by which OSBP inhibition leads to Golgi protein degradation, we explored whether the localization of Golgi proteins is essential for their degradation. Brefeldin A (BFA) was used to redistribute Golgi proteins to the endoplasmic reticulum.[51] Both coincubation of BFA and oxybipin-2 for 18 hours and preincubation of BFA for 2 hours followed by coincubation with oxybipin-2 for 16 hours blocked the degradation of GPP130, indicating that initial Golgi localization is needed for GPP130 degradation (Fig. 6d). Recent preprints suggest that OSBP inhibition leads to the accumulation of excessive PI4P at the TGN and further suppresses normal Golgi function[38,52]. Therefore, a reduction in the levels of PI4P at the TGN may rescue the effect of OSBP inhibition. BF738735, a selective inhibitor of PI4KB, was used to block the synthesis of PI4P at the Golgi. Coincubation of BF738735 with oxybipin-2 markedly attenuated the oxybipins effect on HeLa cell viability (Fig. 6c). In addition, both coincubation of BF738735 with oxybipin-2 for 18 hours and preincubation of BF738735 for 2 hours followed by coincubation with oxybipin-2 for 16 hours rescued the degradation of GPP130 by oxybipin-2 (Fig. 6d). This suggests a mechanistic model where an imbalance of lipids at the Golgi, and particularly the accumulation of PI4P, is responsible for the increased recruitment of OSBP to the Golgi, the degradation of key Golgi proteins and its partial fragmentation on OSBP inhibition (Fig. 6e). This is in line with previous findings where OSW-1 was reported to lead to pronounced changes in cellular membrane lipid order[53]. Notably, PI4KB inhibition rescues this effect at sublethal concentrations (<3 µM), however, at higher concentrations, treatment with BF738735 alone is toxic (Fig. 6c), possibly via excessive reduction of PI4P at the Golgi.

Discussion

Here, we describe the identification of potent and selective chemical tools for inhibiting OSBP, which inhibit retrograde trafficking and Shiga toxin cytotoxicity, as well as exhibiting potent antiproliferative effects against cancer cells. While the original objective of this work was to identify the potential targets of sterols via targeted protein degradation through the synthesis of sterol-containing chemical chimeras, we found that the degradation of GPP130 and a large series of Golgi proteins was a downstream effect of OSBP inhibition, rather than degradation.

Although targeted protein degradation was not a viable strategy for sterol target identification, the identification and comprehensive characterization of the oxybipins as selective OSBP inhibitors provided highly useful tools to study the function of OSBP, as well as its potential as a therapeutic target. So far only a small number of STP inhibitors have been identified, mostly by phenotypic rather than target-based screening and their selectivity profiles have not been studied. Here, we compare oxybipins with other OSBP inhibitors including OSW-1, ITZ, TPP-8307 and THEV2/3/4. Among them, ITZ and TPP-8307 are relatively weak OSBP inhibitors with $IC_{50} > 10$ µM. The natural products termed ORPhilins, including cephalostatin-1, OSW-1 and ritterazine B target OSBP as well as the structurally highly similar ORP4L (ref. 11). However, isolation of these compounds from natural sources is challenging and low yielding, as is their total synthesis[54]. The schweinfürthins are isolable in higher amounts and more amenable to synthesis, however, their selectivity is currently unknown[55,56]. THEV2 exhibits comparable inhibition of OSBP to the oxybipins, however, its weak cellular activity (Extended Data Figs 9 and 10) indicates a potential structural instability, which has previously been attributed to the THP protecting group present in its structure[49], but was not confirmed here. Although THEV3/4 (also known as SR19822 and SR19460, respectively) target OSBP, they were originally reported as inhibitors of ERRγ (ref. 46) and potently inhibit ORP1 and ORP2 (Extended Data Fig. 5h), while being unstable in aqueous solutions (Supplementary Figs. 3 and 4).

By developing recombinant protein assays, HiBit CETSA and iTSA-based intact cell proteomics, we were able to comprehensively explore the selectivity of the oxybipins. This revealed that oxybipin-2 is selective for OSBP, even over the highly similar ORP4L. The establishment of a biophysical selectivity panel will enable the profiling of future STP inhibitors and standardization of activity and selectivity, which was a significant challenge until now.

Oxybipins phenocopy the effects of OSBP mutation, knockdown and inhibition by other OSBP inhibitors on Golgi fragmentation and deglycosylation. OSBP inhibition by OSW-1 has been suggested to inhibit the sialidation and *O*-glycosylation rather than *N*-glycosylation of Golgi proteins, which may explain why PNGase F, tunicamycin and oxybipin-2 cannot induce the same deglycosylation of QSOX2 in our hands[52]. OSBP inhibitors have potential applications in a range of diseases from activity against enteroviruses to specific toxicity toward cancer cell lines. Oxybipins potently inhibit the growth of leukemia cells, in line with recent data for other inhibitors[38]. This effect is dependent on OSBP and was partially rescued by overexpressing OSBP (Fig. 6b). Here, we extend the possible applications to the attenuation of STx cytotoxicity. Currently, the treatment strategies of infections by STx-producing *Escherichia coli* include the neutralization of STx using antibodies[57], inhibiting STx binding with the plasma membrane receptor Gb3 (ref. 58) and blocking the intracellular trafficking route of STx by manganese[13] or Retro-1/2 (ref. 59). Our work further provides an alternative treatment strategy to impair the retrograde trafficking of STx by targeting OSBP. Oxybipins exhibit a significant protective effect against STx at 1 µM without displaying significant toxicity themselves, so long as the treatment time remains short. This suggests a potential therapeutic window for these compounds, which warrants further study.

Online content

Any methods, additional references, Nature Portfolio reporting summaries, source data, extended data, supplementary information, acknowledgements, peer review information; details of author contributions and competing interests; and statements of data and code availability are available at https://doi.org/10.1038/s41589-024-01653-x.

References

1. Luo, J., Yang, H. & Song, B.-L. Mechanisms and regulation of cholesterol homeostasis. *Nat. Rev. Mol. Cell Biol.* **21**, 225–245 (2020).
2. Hulce, J. J., Cognetta, A. B., Niphakis, M. J., Tully, S. E. & Cravatt, B. F. Proteome-wide mapping of cholesterol-interacting proteins in mammalian cells. *Nat. Methods* **10**, 259–264 (2013).
3. Cheng, Y.-S. et al. A proteome-wide map of 20(S)-hydroxycholesterol interactors in cell membranes. *Nat. Chem. Biol.* **17**, 1271–1280 (2021).
4. Rossetti, C. & Laraia, L. Thermal proteome profiling reveals distinct target selectivity for differentially oxidized oxysterols. *ACS Chem. Biol.* **17**, 1677–1684 (2022).
5. Nowak, R. P. & Jones, L. H. Target validation using PROTACs: applying the four pillars framework. *Spec. Issue Adv. Protein Degrad.* **26**, 474–483 (2021).
6. Depta, L., Whitmarsh-Everiss, T. & Laraia, L. Structure, function and small molecule modulation of intracellular sterol transport proteins. *Bioorg. Med. Chem.* **68**, 116856 (2022).
7. Luo, J., Jiang, L.-Y., Yang, H. & Song, B.-L. Intracellular cholesterol transport by sterol transfer proteins at membrane contact sites. *Trends Biochem. Sci.* **44**, 273–292 (2019).
8. Jaworski, C. J., Moreira, E., Li, A., Lee, R. & Rodriguez, I. R. A family of 12 human genes containing oxysterol-binding domains. *Genomics* **78**, 185–196 (2001).

9. Mesmin, B. et al. A four-step cycle driven by PI(4)P hydrolysis directs sterol/PI(4)P exchange by the ER –Golgi tether OSBP. *Cell* **155**, 830–843 (2013).
10. Albulescu, L. et al. Uncovering oxysterol-binding protein (OSBP) as a target of the anti-enteroviral compound TTP-8307. *Antivir. Res.* **140**, 37–44 (2017).
11. Burgett, A. W. G. et al. Natural products reveal cancer cell dependence on oxysterol-binding proteins. *Nat. Chem. Biol.* **7**, 639–647 (2011).
12. Natarajan, R. & Linstedt, A. D. A cycling *cis*-Golgi protein mediates endosome-to-Golgi traffic. *Mol. Biol. Cell* **15**, 4798–4806 (2004).
13. Mukhopadhyay, S. & Linstedt, A. D. Manganese blocks intracellular trafficking of Shiga toxin and protects against Shiga toxicosis. *Science* **335**, 332–335 (2012).
14. Galdeano, C. et al. Structure-guided design and optimization of small molecules targeting the protein–protein interaction between the von Hippel–Lindau (VHL) E3 Ubiquitin Ligase and the Hypoxia Inducible Factor (HIF) alpha subunit with in vitro nanomolar affinities. *J. Med. Chem.* **57**, 8657–8663 (2014).
15. Lu, J. et al. Hijacking the E3 Ubiquitin Ligase cereblon to efficiently target BRD4. *Chem. Biol.* **22**, 755–763 (2015).
16. Yuan, R. et al. Proteasomal inhibition preferentially stimulates lysosome activity relative to autophagic flux in primary astrocytes. *Autophagy* **19**, 570–596 (2023).
17. Furuchi, T., Aikawa, K., Arai, H. & Inoue, K. Bafilomycin A1, a specific inhibitor of vacuolar-type H(+)-ATPase, blocks lysosomal cholesterol trafficking in macrophages. *J. Biol. Chem.* **268**, 27345–27348 (1993).
18. Linstedt, A. D., Mehta, A., Suhan, J., Reggio, H. & Hauri, H. P. Sequence and overexpression of GPP130/GIMPCc: evidence for saturable pH-sensitive targeting of a type II early golgi membrane protein. *Mol. Biol. Cell* **8**, 1073–1087 (1997).
19. Puri, S., Bachert, C., Fimmel, C. J. & Linstedt, A. D. Cycling of early Golgi proteins via the cell surface and endosomes upon lumenal pH disruption. *Traffic* **3**, 641–653 (2002).
20. Mauthe, M. et al. Chloroquine inhibits autophagic flux by decreasing autophagosome–lysosome fusion. *Autophagy* **14**, 1435–1455 (2018).
21. Ronan, B. et al. A highly potent and selective Vps34 inhibitor alters vesicle trafficking and autophagy. *Nat. Chem. Biol.* **10**, 1013–1019 (2014).
22. Neklesa, T. K. et al. Small-molecule hydrophobic tagging-induced degradation of HaloTag fusion proteins. *Nat. Chem. Biol.* **7**, 538–543 (2011).
23. Wang, T.-E. et al. Mouse quiescin sulfhydryl oxidases exhibit distinct epididymal luminal distribution with segment-specific sperm surface associations. *Biol. Reprod.* **99**, 1022–1033 (2018).
24. Hirst, J., Itzhak, D. N., Antrobus, R., Borner, G. H. H. & Robinson, M. S. Role of the AP-5 adaptor protein complex in late endosome-to-Golgi retrieval. *PLoS Biol.* **16**, e2004411 (2018).
25. Mukhopadhyay, S., Bachert, C., Smith, D. R. & Linstedt, A. D. Manganese-induced trafficking and turnover of the *cis*-Golgi Glycoprotein GPP130. *Mol. Biol. Cell* **21**, 1282–1292 (2010).
26. Tewari, R., Bachert, C. & Linstedt, A. D. Induced oligomerization targets Golgi proteins for degradation in lysosomes. *Mol. Biol. Cell* **26**, 4427–4437 (2015).
27. Mustonen, V., Muruganandam, G., Loris, R., Kursula, P. & Ruskamo, S. Crystal and solution structure of NDRG1, a membrane-binding protein linked to myelination and tumour suppression. *FEBS J.* **288**, 3507–3529 (2021).
28. Adolf, F. et al. Proteomic profiling of mammalian COPII and COPI vesicles. *Cell Rep.* **26**, 250–265.e5 (2019).
29. Nishimura, T. et al. Oxysterol-binding protein (OSBP) is required for the perinuclear localization of intra-Golgi v-SNAREs. *Mol. Biol. Cell* **24**, 3534–3544 (2013).
30. Zhan, Z. et al. Anticancer effects and mechanisms of OSW-1 isolated from *Ornithogalum saundersiae*: a review. *Front. Oncol.* **11**, 747718 (2021).
31. Kimura, M. et al. Anticancer saponin OSW-1 is a novel class of selective Golgi stress inducer. *Bioorg. Med. Chem. Lett.* **29**, 1732–1736 (2019).
32. Taskinen, J. H., Ruhanen, H., Matysik, S., Käkelä, R. & Olkkonen, V. M. Global effects of pharmacologic inhibition of OSBP in human umbilical vein endothelial cells. *Steroids* **185**, 109053 (2022).
33. Tong, J., Manik, M. K. & Im, Y. J. Structural basis of sterol recognition and non-vesicular transport by lipid transfer proteins anchored at membrane contact sites. *Proc. Natl Acad. Sci. USA* **115**, E856–E865 (2018).
34. Horenkamp, F. A., Valverde, D. P., Nunnari, J. & Reinisch, K. M. Molecular basis for sterol transport by StART-like lipid transfer domains. *EMBO J.* **37**, e98002 (2018).
35. Thorsell, A.-G. et al. Comparative structural analysis of lipid binding START domains. *PLoS ONE* **6**, e19521 (2011).
36. Whitmarsh-Everiss, T., Olsen, A. H. & Laraia, L. Identification of inhibitors of cholesterol transport proteins through the synthesis of a diverse, sterol-inspired compound collection. *Angew. Chem. Int. Ed.* **60**, 26755–26761 (2021).
37. Laraia, L. et al. The cholesterol transfer protein GRAMD1A regulates autophagosome biogenesis. *Nat. Chem. Biol.* **15**, 710–720 (2019).
38. Cigler, M. et al. Orpinolide disrupts a leukemic dependency on cholesterol transport by inhibiting OSBP. *Nat. Chem. Biol.* https://doi.org/10.1038/s41589-024-01614-4 (2024).
39. Severance, Z. C. et al. Structure–activity relationships of ligand binding to oxysterol-binding protein (OSBP) and OSBP-related protein 4. *J. Med. Chem.* **66**, 3866–3875 (2023).
40. Ball, K. A. et al. An isothermal shift assay for proteome scale drug-target identification. *Commun. Biol.* **3**, 75 (2020).
41. Jarzab, A. et al. Meltome atlas—thermal proteome stability across the tree of life. *Nat. Methods* **17**, 495–503 (2020).
42. Li, J., Van Vranken, J. G., Paulo, J. A., Huttlin, E. L. & Gygi, S. P. Selection of heating temperatures improves the sensitivity of the proteome integral solubility alteration assay. *J. Proteome Res.* **19**, 2159–2166 (2020).
43. Arita, M. et al. Oxysterol-binding protein family I is the target of minor enviroxime-like compounds. *J. Virol.* **87**, 4252–4260 (2013).
44. Kobayashi, J. et al. Ligand recognition by the lipid transfer domain of human OSBP is important for enterovirus replication. *ACS Infect. Dis.* **8**, 1161–1170 (2022).
45. Strating, J. R. P. M. et al. Itraconazole inhibits enterovirus replication by targeting the oxysterol-binding protein. *Cell Rep.* **10**, 600–615 (2015).
46. Lin, H. et al. Design, synthesis, and evaluation of simple phenol amides as ERRγ agonists. *Bioorg. Med. Chem. Lett.* **28**, 1313–1319 (2018).
47. Long, T. et al. Structural basis for itraconazole-mediated NPC1 inhibition. *Nat. Commun.* **11**, 152 (2020).
48. Nhek, S. et al. Regulation of oxysterol-binding protein Golgi localization through protein kinase D-mediated phosphorylation. *Mol. Biol. Cell* **21**, 2327–2337 (2010).
49. Roberts, B. L. et al. Differing activities of oxysterol-binding protein (OSBP) targeting anti-viral compounds. *Antivir. Res.* **170**, 104548 (2019).
50. Stechmann, B. et al. Inhibition of retrograde transport protects mice from lethal Ricin challenge. *Cell* **141**, 231–242 (2010).
51. Lippincott-Schwartz, J., Yuan, L. C., Bonifacino, J. S. & Klausner, R. D. Rapid redistribution of Golgi proteins into the ER in cells treated with brefeldin A: evidence for membrane cycling from Golgi to ER. *Cell* **56**, 801–813 (1989).

52. Sasaki, K. et al. The cholesterol pathway of the Golgi stress response induces cell death and transcription of Golgi-related genes through metabolic dysregulation of phosphatidylinositol-4-phosphate. Preprint at *bioRxiv* https://doi.org/10.1101/2023.05.18.541279 (2023).
53. Mesmin, B. et al. Sterol transfer, PI4P consumption, and control of membrane lipid order by endogenous OSBP. *EMBO J.* **36**, 3156–3174 (2017).
54. Nakayama, Y. et al. Total synthesis of Ritterazine B. *J. Am. Chem. Soc.* **143**, 4187–4192 (2021).
55. Péresse, T. et al. Molecular and cellular dissection of the oxysterol-binding protein cycle through a fluorescent inhibitor. *J. Biol. Chem.* **295**, 4277–4288 (2020).
56. Jézéquel, G. et al. Structure-based design of a lead compound derived from natural Schweinfurthins with antitumor properties that target oxysterol-binding protein. *J. Med. Chem.* **66**, 14208–14220 (2023).
57. Cheng, L. W., Henderson, T. D., Patfield, S., Stanker, L. H. & He, X. Mouse in vivo neutralization of *Escherichia coli* Shiga toxin 2 with monoclonal antibodies. *Toxins* **5**, 1845–1858 (2013).
58. Mühlen, S. & Dersch, P. Treatment strategies for infections with Shiga toxin-producing *Escherichia coli*. *Front. Cell. Infect. Microbiol.* **10**, 169 (2020).
59. Forrester, A. et al. Functional dissection of the retrograde Shiga toxin trafficking inhibitor Retro-2. *Nat. Chem. Biol.* **16**, 327–336 (2020).

Methods

Chemical synthesis

All synthetic procedures are available in the Supplementary Information. Nuclear magnetic resonance spectra were analyzed with MestreNova, v.x64.

Cell culture

The reagents used for cell culture and proteomics can be found in Supplementary Table 1. The A549 and HeLa cells were cultured in DMEM supplemented with 10% FBS and 1% penicillin–streptomycin at 37 °C with 5% CO_2. Jurkat and MOLM13 were cultured in RPMI supplemented with 10% FBS and 1% penicillin–streptomycin at 37 °C with 5% CO_2. KBM7 WT (wild type) (obtained from T. Brummelkamp's laboratory) as well as cells expressing HiBiT- or HA-tagged ORPs (generated as reported in ref. 38) were cultured in IMDM with 10% FBS and 1% penicillin–streptomycin at 37 °C with 5% CO_2.

Cell lysis and sample preparation for mass spectrometry analysis

For expression proteomics of 1–8, Mn^{2+} and OSW-1. Here, 2 ml of cells (cell density 2×10^5 cells per ml) were seeded in six-well plates and incubated overnight at 37 °C and 5% CO_2. The following day, cells were incubated with the corresponding compound (or DMSO for the control sample) for 18 h at 37 °C and 5% CO_2. At the end of the incubation, cells were washed with ice-cold PBS twice and lysed by the addition of lysis buffer consisting of 0.4% (v/v) NP-40 in PBS on ice.

For oxybipin-2 iTSA. Two six-well plates were seeded with each 3×10^5 HeLa cells in 2 ml of DMEM per well and incubated at 37 °C and 5% CO_2 overnight. The following day, cells were incubated with the corresponding compound (or DMSO for the control sample) for 0.5 h. At the end of the incubation, cells were detached using 200 µl of trypsin and collected in 0.5 ml of MEM each. Treated and nontreated cell suspensions were centrifuged (350*g*, 5 min), and resuspended in 50 µl of PBS in PCR tubes. The samples were heated at 53 °C (Eppendorf Mastercycler ep Gradient S). After the heat treatment, 5 µl of PBS containing 4.4% (v/v) NP-40 were added to each sample.

Sample preparation. Lysis was finalized by four freeze–thaw cycles using liquid nitrogen. Cellular debris were removed by centrifugation at 25,000*g* for 25 minutes at 4 °C. The protein concentration of the cell lysate was measured by DC assay (Bio-Rad) and further diluted to a protein concentration of 2 mg ml^{-1} in lysis buffer.

For each sample, 150 µg of total proteins were further diluted in 100 mM TEAB, and with 200 mM TCEP for cysteine reduction for 1 h at 55 °C. Then 375 mM IAA was successively used for alkylation for 30 min at room temperature in the dark. After this step, proteins were precipitated overnight with 6 volumes of cold acetone at −20 °C. The following day, the protein pellets were collected by centrifugation at 8,000*g* at 4 °C for 10 min and resuspended in TEAB 100 mM before digestion. Protein digestion was performed by adding trypsin in a 1/80 enzyme to substrate ratio and left overnight at 37 °C, with gentle shaking in a ThermoMixer (Eppendorf). Half of the sample volume corresponding to 75 µg of peptides were successively labeled with TMT 11-plex or TMTpro 16plex reagents kits. Experimental replicates were labeled with different TMT batches concatenated by a pooled internal reference sample for each TMT batch, which consisted of an additional sample obtained by pooling equal amounts of each sample from the same TMT batch. The TMT reaction was allowed for 2 h and quenched with 5% hydroxylamine. All samples related to each batch were pooled and dried in SpeedVac (Eppendorf, catalog no. EP022822993) before desalting with Sep-Pak Plus C18 cartridges. Peptides were eluted with 40 and 60% of acetonitrile in 0.1% of trifluoroacetic acid and dried before injection of 30 µg in the ultrahigh-performance liquid chromatography (UHPLC) system (Dionex, catalog no. U3000) for high-pH fractionation.

The separation of the peptides was carried out at a constant flowrate of 5 µl min^{-1} on a CSH C18 Acquity UPLC M-Class Peptide column, 130 Å, 1.7 µm, 300 µm × 150 mm (Waters, catalog no. 186007563) using a 100 min linear gradient from 5 to 35% of mobile phase B (acetonitrile) with a subsequent 15 min gradient to 70%, before 5 min of re-equilibration with 95% of mobile phase A (5 mM ammonium bicarbonate, pH 10). Then, 60 time-based fractions were pooled in 30 fractions in the collection plates. Clean-up of the fractions was performed by EvoTip according to the manufacturer's instructions.

Liquid chromatography with mass spectrometry analysis

The EvoTips (EvoSep, catalog no. EV2003) were loaded on the Evosep One module (EvoSep, catalog no. EV-1000) coupled to an Orbitrap Eclipse Tribid mass spectrometer (ThermoFisher Scientific). Peptides were loaded onto the EASY-Spray C18 column, 2 µm, 100 Å, 75 µm × 15 cm (ThermoFisher Scientific, catalog no. ES804) using the standard '30 samples per day' Evosep method. The method eluted the peptides with a 44 min gradient ranging from 5 to 90% acetonitrile with 0.1% formic acid. The mass spectrometry acquisition was performed in data dependent-MS3 with real-time search (RTS) and a field asymmetric ion mobility spectrometry interface switching between compensation voltages of −50 and −70 V with cycle times of 2 and 1.5 s, respectively. The data dependent acquisition mode was run in a MS1 scan range between 375 and 1,500 *m/z* with a resolution of 120,000, and a normalized gain control (AGC) target of 100%, with a maximum injection time of 50 ms. The RF lens set at 30%. Filtering of the precursors was performed using peptide monoisotopic peak selection, including charge states from 2 to 7, dynamic exclusion of 120 s with ±10 ppm tolerance excluding isotopes and a precursor fit of 70% in a window of 0.7 *m/z* with an intensity threshold of 5,000. Selected precursors for further MS2 analysis were isolated with a window of 0.7 *m/z* in the quadrupole. The MS2 scan was performed over a range of 200–1,400 *m/z*, collecting ions with a maximum injection time of 35 ms and normalized AGC target of 300% MS2 fragmentation was operated with normalized higher-energy collisional dissociation collision energy at 30%. Fragmentation spectra were searched against the fasta files from the human UniProt database (reviewed) in the RTS, set with tryptic digestion, TMT11-plex as fixed modification on Lysine (K) and N terminus together with cysteine (C) carbamidomethylation and oxidation of methionine (M) as variable modification. One missed cleavage and two variable modifications were allowed with a maximum search time of 35 ms. False discovery rate (FDR) filtering was enabled with 1 as Xcorrelation and 5 ppm of precursor tolerance. Precursors identified via RTS in the MS2 scan were further isolated in the quadrupole with a 2 *m/z* window, maximum injection time of 86 ms and normalized AGC target of 300%. The further MS3 fragmentation was operated with a normalized higher-energy collisional dissociation collision energy at 50% and fragments were scanned with a resolution of 50,000 in the range of 100 to 500 *m/z*. The mass spectrometry performances were monitored by quality control of an in-house standard of HeLa cell lysate, both at the beginning and the end of each sample set.

Data analysis

For TMT11 labels, mass spectrometric raw files were analyzed with MaxQuant (v.1.6.2.10, https://maxquant.org/) setting all the TMT11 labels as reporter ion MS3 for lysine and N terminus with mass tolerance 0.003 Da. The search settings included carbamidomethylation of cysteine (C) as fixed modifications, methionine (M) oxidation and acetylation of protein N termini as variable modification and trypsin as enzyme (allowing a maximum of two missed cleavages). Peptide–spectrum match and protein FDRs were 0.01 with at least one minimum razor + unique peptides. Peptide sequences were searched against UniProtKB/TrEMBL human proteome6 fasta file (downloaded on 8 August 2018, https://www.uniprot.org/proteomes/). The protein group file generated from the MaxQuant analysis were processed for further normalization and scaling.

For TMTpro labels, mass spectrometric raw files were analyzed with Proteome Discoverer v.2.4 (Thermo Fisher Scientific) by using the built-in TMTpro Reporter ion standard quantification workflows. The search was run setting trypsin as enzyme (allowing a maximum of two missed cleavages), TMTpro16plex and carbamidomethylation of cysteine (C) as fixed modifications, while methionine (M) oxidation and acetylation of protein N termini as variable modifications. The Sequest search engine was used to match the MS2 spectra in the UniProt homo sapiens database (Swiss-Prot reviewed including isoforms) with a precursor mass tolerance of 10 ppm and fragment mass tolerance of 0.6 Da. Percolator was used to score the results and to filter at 1% FDR. Reporter ion quantification was performed on MS2 spectra by applying isotopic error correction. Normalization and scaling were not included in the Proteome Discovery analysis and were performed successively on the protein result table.

Here, in the first step, contaminant proteins and proteins not identified as Master Protein or as Master Protein Candidate were removed. Moreover, all the proteins identified with a sum of Unique + Razor peptides below 2 were removed. Loading normalization was performed summing the intensities for each TMT channel and calculating the respective correction factor on the average of the summed intensities. Hence, each protein intensity was normalized for the respective channel correction factor.

Normalized intensities were further considered to calculate the average among the replicates and the FCs for compound-treated samples over the control samples. Only proteins identified in all three replicates were used for further analysis. The obtained values were $\log_2$ transformed. *P* values were determined by a Student's two-tailed *t*-test assuming equal variances from the data of three replicates and obtained *P* values were $-\log_{10}$ transformed.

Volcano plots were obtained plotting the $\log_2$ FC versus $-\log_{10} P$ in both Prism v.5 (Graphpad Software, Inc. v.5.3).

Immunoblotting. The antibodies used for immunoblotting can be found in Supplementary Table 2. For degradation tests, 2×10^5 cells per ml A549 and HeLa cells in 2 ml of medium were seeded in six-well plates and incubated (37 °C and 5% CO_2) overnight. The media was then removed and replaced with the fresh media containing the required concentration of compounds dissolved in DMSO. At the specific time point, cells were washed with ice-cold PBS twice and then lysed in lysis buffer (100 mM Tris-HCl (pH 6.8), 4% (w/v) sodium dodecyl sulfate (SDS), 20% (v/v) glycerol) and sonicated by ultrasonic processor (UP100H, Hielscher). The protein concentrations of the lysate were determined using NanoDrop ND-1000 spectrophotometer (Saveen Werner ABn) according to the manufacturer's instructions and further diluted to 4 mg ml^{-1}. SDS–PAGE was carried out using 4–15 or 4–20% precast polyacrylamide gels (Bio-Rad, catalog nos. 4561086 or 4561093) and run at a constant voltage of 80 V for 5 min followed by 120 V for 1 h. Semidry transfer onto a polyvinyl difluoride membrane was performed using Bio-Rad Trans-Blot Turbo Transfer System at 1.3 A for 7 min. For chemiluminescent detection, membranes were blocked in 5% milk in TBST (tris-buffered saline with Tween) (137 mM NaCl, 19 mM Tris-base, 2.7 mM KCl and 0.1% (v/v) Tween-20, blocking buffer) for 1 h at room temperature. The membrane was incubated with the primary antibody in blocking buffer overnight at 4 °C. After washing with TBST (3 × 5 min), the membrane was incubated with the secondary antibody in blocking buffer for 1 h at room temperature. Signals were visualized using the SuperSignal West Pico Chemiluminescent Substrate (Thermo Fisher, catalog no. 34579) or the SuperSignal West Femto Maximum Sensitivity Substrate (Thermo Fisher, catalog no. 34094) on a Li-COR Odyssey Fc. For fluorescent detection, membranes were blocked in Intercept (TBS) Blocking Buffer (Li-COR, catalog no. 927-60001) for 1 h at room temperature. The membrane was incubated with the primary antibody in blocking buffer overnight at 4 °C. After washing with TBST (3 × 5 min), the membrane was incubated with the secondary antibody in blocking buffer for 1 h at room temperature. Signals were visualized on a Li-COR Odyssey Fc.

In-cell CETSA. Two T75 cell culture flasks were seeded with each 6×10^5 HeLa cells in media and incubated at 37 °C and 5% CO_2 for 3 days. The media was then removed and replaced with 3 ml of medium containing either 10 µM of the given compound or DMSO. After incubation for 1 h at 37 °C and 5% CO_2 the medium was removed and the cells were washed by PBS and detached using 1.5 ml of trypsin. Then, the media and trypsin were removed by centrifuge at 250*g* for 3 min. After three times washing by PBS, 1×10^6 cells were collected in 0.6 ml of PBS each. Treated and nontreated cell suspensions were divided into ten aliquots, each 100 µl in PCR tubes. The aliquots were individually heated at different temperatures (Doppio 2×48 well Thermal cycler, VWR). After the heat treatment, 10 µl of PBS containing 4.4% (v/v) NP-40 added to each sample and cells were lysed by freeze–thaw four times. The cell lysates were completely transferred to polycarbonate tubes and centrifuged (Micro Star 30, VWR) at 25,000*g*, 4 °C for 25 min. The cleared supernatants were collected and further analyzed by western blotting assay.

In-cell ITDRF experiments. Two six-well plates were seeded with each 3×10^5 HeLa cells in 2 ml of DMEM per well and incubated at 37 °C and 5% CO_2 overnight. The media was subsequently removed and replaced with 0.5 ml of medium containing either different concentrations (40, 20, 10, 5, 2.5, 1.25, 0.625, 0.3 µM) of the test compound or DMSO. After incubation for 1 h at 37 °C and 5% CO_2, the medium was removed and cells were detached using 200 µl of trypsin and collected in 0.5 ml of MEM each. Treated and nontreated cell suspensions were centrifuged (350*g*, 5 min), and resuspended in 50 µl of PBS in PCR tubes. The samples were heated at the given temperature (Eppendorf Mastercycler ep Gradient S). After the heat treatment, 5 µl of PBS containing 4.4% (v/v) NP-40 were added to each sample and cells lysed by freeze and thaw four times and then the cell lysates were completely transferred to polycarbonate tubes and centrifuged (Micro Star 30, VMR) at 25,000*g*, 4 °C for 25 min. The cleared supernatants were collected and further analyzed by western blotting assay.

Cell lysate CETSA. HeLa cell lysates (protein concentration 2 mg ml^{-1}) were separated in the two aliquots (1.0 ml) to be incubated for 10 min at room temperature with either 0.1% DMSO (1.0 µl) or with 10 µM of the tested compound. After incubation, each aliquot (each 100 µl) was heated at different temperatures for 3 min using PCR gradient cyclers. After heating, the removal of the precipitated proteins from the solution was performed by ultracentrifugation at 4 °C with a speed of 25,000*g* for 25 min. The cleared supernatants were collected and further analyzed by western blotting.

Cell lysate ITDRF experiments. HeLa lysates (protein concentration 2 mg ml^{-1}) were separated in nine aliquots (each 100 µl) to be incubated for 10 min at room temperature with either 0.1% DMSO or with decreasing concentration of the tested compounds (40, 20, 10, 5, 2.5, 1.25, 0.625, 0.3 µM). All the aliquots were successively heated for 3 min at the given temperature using PCR gradient cyclers. After heating, the removal of the precipitated proteins from the solution was performed by ultracentrifugation at 4 °C with a speed of 25,000*g* for 25 min. The cleared supernatants were collected and further analyzed by western blotting.

Deglycosylation assay. HeLa cell lysates were incubated with PNGase F (New England Biolabs, catalog no. NEB-P0704S) according to the manufacturer's instructions. Briefly, 10 µl of reaction mixture (9 µl of 1 mg ml^{-1} HeLa cell lysate and 1 µl of Glycoprotein Denaturing Buffer (10×)) was denatured by heating at 100 °C for 10 min. The denatured protein mixture was chilled on ice and centrifuged for 10 s. Then, 2 µl of GlycoBuffer 2 (10×), 2 µl of 10% NP-40, 6 µl of H_2O were added to the previous reaction mixture to make a total reaction volume of 20 µl. Next, 1 µl PNGase F was added to the reaction mixture and the mixture was incubated at 37 °C for 2 h and analyzed by western blotting as previously described.

Protein expression. *Protein expression constructs*. Human ASTER domains of Aster-A(359-547), -B(364-552) and -C(318-504) were subcloned into a pGEX-6p-2rbs vector, thus introducing the cloning artifact 'GPLGS'. The pGEX-6P-1-GST-OSBP(377-807), pET24b(+)-ORP1(534-950) and pET24b(+)-ORP2(49-480) plasmids were purchased from Genscript. The pET22b_His6_STARD1(66-284) plasmid was a gift from J.H. Hurley (University of California).

Protein expression and purification. ASTER domains of human Aster-A(359-547), -B(364-552) and -C(318-504) in the pGEX-6p-2rps vector with an N-terminal PreScission-cleavable GST tag were expressed in *E. coli* OverExpress C41 in Terrific Broth medium for approximately 16 h at 18 °C after induction with 0.1 mM isopropyl-β-D-thiogalactoside (IPTG). Cells were collected at 3,500*g* for 15 min and lysed by sonication in buffer containing 50 mM HEPES pH 7.5, 300 mM NaCl, 10% (vol/vol) glycerol, 5 mM dithiothreitol (DTT), 0.1% (vol/vol) Triton X-100 and protease inhibitor mix HP plus (Serva). The cleared lysate was purified by affinity chromatography on a GSTrap FF column (Cytiva) using an ÄKTA Start (Cytiva) in buffer containing 50 mM HEPES pH 7.5, 300 mM NaCl, 10% (vol/vol) glycerol, 5 mM DTT and 0.01% (vol/vol) Triton X-100. The GST tag was cleaved on the column overnight at 4 °C. Proteins were further purified by size-exclusion chromatography on a HiLoad 16/600 Superdex 75 pg (Cytiva) in buffer containing 20 mM HEPES pH 7.5, 300 mM NaCl, 10% (vol/vol) glycerol and 2 mM DTT.

The START domain of human STARD1(66-284) harboring an N-terminal His6-Tag was expressed in *E. coli* BL21(DE3) in Luria-Bertani (LB) medium for approximately 16 h at 18 °C after induction with 0.15 mM IPTG. Cells were collected at 3,500*g* for 15 min and lysed by sonication in buffer containing 50 mM HEPES pH 7.5, 150 mM NaCl, 5% (vol/vol) glycerol, 5 mM DTT, 0.1% (vol/vol) Triton X-100 and EDTA-free protease inhibitor cocktail (Sigma-Aldrich). The cleared lysate was purified by affinity chromatography on a Ni-NTA Superflow Cartridge (Qiagen) using an ÄKTA Start (Cytiva) in buffer containing 50 mM HEPES pH 7.5, 150 mM NaCl, 5% (vol/vol) glycerol, 5 mM DTT. START domains were eluted by using elution buffer containing 50 mM HEPES pH 7.5, 150 mM NaCl, 5% (vol/vol) glycerol, 5 mM DTT and 500 mM imidazole. Proteins were further purified by size-exclusion chromatography on a HiLoad 16/600 Superdex 75 pg (Cytiva) in buffer containing 20 mM HEPES pH 7.5, 150 mM NaCl, 5% (vol/vol) glycerol and 2 mM DTT.

The ORP domain of human OSBP(377-807) in the pGEX-6p-1 vector with an N-terminal PreScission-cleavable GST tag was expressed in *E. coli* OverExpress C41 in LB medium for approximately 16 h at 18 °C after induction with 0.1 mM IPTG. Cells were collected at 3,500*g* for 15 min and lysed by sonication in buffer containing 20 mM HEPES pH 7.5, 300 mM NaCl, 10% (vol/vol) glycerol, 5 mM DTT, 0.1% (vol/vol) Triton X-100 and EDTA-free protease inhibitor cocktail (Sigma-Aldrich). The cleared lysate was purified by affinity chromatography on a GSTrap HF column (Cytiva) using an ÄKTA Start (Cytiva) in buffer containing 20 mM HEPES pH 7.5, 300 mM NaCl, 10% (vol/vol) glycerol, 5 mM DTT. OSBP(377-807) was eluted by using elution buffer containing 20 mM HEPES pH 7.5, 300 mM NaCl, 10% (vol/vol) glycerol, 5 mM DTT and 10 mM reduced glutathione. Proteins were further purified by size-exclusion chromatography on a HiLoad 16/600 Superdex 75 pg (Cytiva) using an ÄKTA Explorer (Cytiva) in buffer containing 20 mM HEPES pH 7.5, 150 mM NaCl, 10% (vol/vol) glycerol and 2 mM DTT.

The ORP domain of human ORP1(534-950) in pET24b(+) and ORP2(49-480) in the pET24b(+) vector including an N-terminal His6-Tag were expressed in *E. coli* BL21(DE3) in Terrific Broth medium for approximately 16 h at 18 °C after induction with 0.1 mM IPTG. Cells were collected at 3,500*g* for 15 min and lysed by sonification in buffer containing 10 mM Tris-HCl pH 8, 300 mM NaCl, 5% glycerol, 2 mM DTT, 0.1% Triton X-100 and EDTA-free protease inhibitor cocktail (Sigma-Aldrich). The cleared lysate was purified by affinity chromatography on a Ni-NTA Superflow Cartridge (Qiagen) using an ÄKTA Start (Cytiva) in buffer containing 10 mM Tris-HCl, pH 8, 300 mM NaCl, 5% glycerol, 2 mM DTT. ORP domains were eluted using elution buffer containing 10 mM Tris-HCl, pH 8, 300 mM NaCl, 5% glycerol, 500 mM imidazole, 2 mM DTT. The proteins were further purified by size-exclusion chromatography on a HiLoad 16/600 Superdex 75 pg (Cytiva) using an ÄKTA Explorer (Cytiva) in buffer containing 10 mM Tris-HCl, pH 8, 150 mM NaCl, 5% glycerol and 2 mM DTT.

FP. FP experiments were performed in a buffer composed of 20 mM HEPES pH 7.5, 300 mM NaCl, 0.01% (vol/vol) Tween-20, 0.5% glycerol and 2 mM DTT in a final volume of 30 µl in black, flat-bottom, nonbinding 384-well plates (Corning). For competition experiments, 20 nM 22-NBD-cholesterol or 80 nM 25-NBD-cholesterol was mixed with protein and incubated with desired concentrations of screening compounds. The FP signal was measured using a Spark Cyto multimode microplate reader (Tecan) with filters set at 485 ± 20 nm for excitation and at 535 ± 20 nm for emission. The data were analyzed using GraphPad Prism 5. Measured mP values were normalized setting 100% inhibition as the FP signal from the protein + fluorophore control well and 0% as the FP signal from the fluorophore control well. Curves were fitted to the normalized data via nonlinear regression to allow the determination of IC_{50} values. The detailed conditions used for FP can be found in Supplementary Table 3.

Sterol transfer assay. *Preparation of vesicles*. Here, 1,2-dioleoyl-*sn*-glycero-3-phosphocholine (DOPC, Avanti Polar Lipids, catalog no. 850375C) was prepared in chloroform (10 mg ml^{-1}); 23-(dipyrrometheneboron difluoride)-24-norcholesterol (TopFluor Cholesterol, Avanti Polar Lipids, catalog no. 810255) and *N*-(lissamine rhodamine B sulfonyl)-1,2-dihexadecanoyl-*sn*-glycero-3-phosphoethanolamine (triethylammonium salt) (Rh-DHPE, Invitrogen, catalog no. L1392) were prepared in methanol (100 µM). The acceptor liposomes (L_A) consist of DOPC only while the donor liposomes (L_D) consist of a mixture of DOPC:TF-Chol:Rh-DHPE (99:0.5:0.5). The solvent was evaporated under a stream of nitrogen, followed by drying under vacuum overnight. The lipid films were hydrated to a final concentration of 60 µM using buffer containing 20 mM HEPES pH 7.5, 300 mM NaCl and 2 mM DTT. To fully dissolve the lipid films the solutions were vortexed and sonicated for 5 min in a 40 °C water bath, followed by five freeze–thaw cycles in liquid nitrogen. Extrusion through a polycarbonate membrane (21 times, 0.1 µM pore size, Avanti Polar Lipids) at 40 °C yielded homogenous unilamellar vesicles, which were kept on ice and used on the same day.

Microplate-based cholesterol transfer assay. GST-tagged OSBP(377-807) with a final concentration of 500 nM was preincubated with either DMSO or compound from a 10 mM stock solution in DMSO at room temperature for 30 min in buffer (20 mM HEPES pH 7.5, 300 mM NaCl, 2 mM DTT). The measurements were carried out in nonbinding clear-bottom 96-well plates (Greiner Bio-One, catalog no. 655906). Equal amounts of L_A and L_D were added to the wells (16 µM). After 2.5 min of FRET signal measurement GST-OSBP(377-807) preincubated with DMSO or compound was added and rapidly mixed using a pipette. Control wells contained the L_A/L_D mixture only. FRET signal was measured using a Tecan Spark Cyto plate reader, with readings from the bottom of the wells every 10 s for 15 min. The excitation monochromator was set at 488 ± 20 nm and the emission monochromator at 590 ± 20 nm.

DLS. Before the DLS experiments, GST-tagged OSBP(377-807) was purified via size-exclusion chromatography (HiLoad 16/600 Superdex 75 pg (Cytiva)) using an ÄKTA Explorer (Cytiva) in buffer containing 20 mM HEPES pH 7.5, 150 mM NaCl, 10% (vol/vol) glycerol and 2 mM DTT. After filtration through a 0.2 µm pore size filter (catalog no. 6876-2502, Whatman, GE Healthcare Life Sciences)) the protein (1 µM) was preincubated with DMSO or compound (1 µM). The measurements were carried out in polystyrene cuvettes (67.741, Sarstedt) using the Zetasizer Nano (Malvern) to measure the particle sizes.

Controls included measurements of buffer only as well compounds in buffer and DMSO in buffer without the protein. The data were plotted as volumes versus size using the software Prism 9 (Graphpad Software Inc., v.9.41).

HiBiT CETSA in intact cells. After treatment with test compounds or DMSO (1 million cells per ml), KBM7 cells overexpressing HiBiT-tagged ORPs (generated as reported in Cigler et al.)[38] were spun down (1,450 rpm, 5 min), washed once with PBS and resuspended in PBS (100 µl of PBS per 1 million cells). The cell suspension (100 µl) was distributed into PCR strips, spun down (1,450 rpm, 5 min) and 80 µl of the supernatant were removed without disturbing the cell pellet. The samples were then thermally destabilized (3 min temperature gradient of choice followed by 3 min at 25 °C) and resuspended in 30 µl of the lysis buffer (20 mM Tris-HCl pH 8.0, 120 mM NaCl, 0.5% NP-40). Three freeze–thaw cycles with liquid nitrogen were then performed and the lysed samples were cleared out via centrifugation (20,817*g*, 20 min, 4 °C).

Luminescence was assessed with the Nano-Glo HiBiT Lytic Detection System (Promega, N3040) in 384-well plate format and in technical triplicates. Briefly, a 6× detection master mix was prepared containing the substrate, LgBiT and the provided lysis buffer and 2.5 µl were distributed into well plates. Cleared lysates of cells expressing HiBiT-tagged ORPs (12.5 µl) were then added into respective wells and the plates were incubated at room temperature for 10 min with mild shaking. Luminescence signal was measured on the Multilabel Plate Reader Platform Victor X3 model 2030 (Perkin Elmer). Melting curves and T_m were determined in GraphPad Prism (v.9.5.1) by fitting a nonlinear regression curve or interpolation of a sigmoidal standard curve. Each data point was normalized to the mean luminescence at the lowest temperature (37.6 °C).

Cell viability assay. Adherent cells (HeLa) cells were cultivated in a T175 flask and gathered (70% confluence) by trypsinization and diluted to 3×10^4 cells per ml medium. Then, 100 µl per well of the cell suspension were transferred into a 96-well plate (Nunc Edge, clear, 167425, Thermo Fisher) and incubated overnight (37 °C, 5% CO$_2$) to allow attachment. After 24 h, the media was removed and a dilution series of compounds in 100 µl of DMEM medium (10% FBS, 1% PS) was added. Suspension cells (Jurkat and MOLM13) were cultivated in T175 flasks and collected by centrifugation (1,000 rpm, 5 min, room temperature) and diluted to 5×10^4 cells per ml of medium. Next, 50 µl per well of the cell suspension were transferred into a 96-well plate (Nunc Edge, clear, 167425, Thermo Fisher). A dilution series of the compounds in 50 µl of DMEM medium (10% FBS, 1% PS) was added immediately. After 72 h of incubation (37 °C, 5% CO$_2$) cell viability was determined by using the Cell Titer Blue Assay kit (G8080, Promega). According to the manufacturer's instructions, 10 µl of Cell Titer Blue reagent were added to each well followed by an incubation time of 60 min at 37 °C. Afterward, fluorescence intensity was measured using a Tecan Spark Cyto plate reader with excitation filters set to 560 ± 20 nm and emission filter set to 590 ± 20 nm. Cell viability of KBM7 WT and OSBP(WT)-2HA overexpressing cells was assessed with the CellTiter-Glo assay (Promega, catalog no. G7573) according to the manufacturer's protocol. Luminescence signal was measured on the Multilabel Plate Reader Platform Victor X3 model 2030 (Perkin Elmer). Controls included wells with medium only for background subtraction as well as DMSO and medium containing wells for signal normalization. Data analysis was performed using the software Prism 9 (Graphpad Software, Inc. v.9.41).

Shiga toxin trafficking assay. HeLa cells were seeded 1 day before use, and used at 70% confluency. Cells were treated for 4 h with 1 µM of each compound or DMSO vehicle, in complete media at 37 °C. Media was changed to fresh media containing 0.5 µg ml^{-1} STxB-488 (a gift from L. Johannes, Institut Curie, Paris) and compounds as before. HeLa cells were incubated at 37 °C for 40 min, then fixed in 4% PFA for 10 min at room temperature. Immunofluorescence was performed.

Golgi fragmentation assay. HeLa cells were used at 70% confluency. Cells were treated with compounds or DMSO vehicle for 4 h at 37 °C, then fixed with 4% PFA for 10 min at room temperature, followed by immunofluorescence analysis.

Immunofluorescence. Fixed cells were blocked and permeabilized for 20 min in blocking buffer (0.05% (w/v) saponin, 0.5% (w/v) BSA, 50 mM NH$_4$Cl and 0.02% NaN$_3$ in PBS, pH 7.4). Cells were incubated for 1 h with primary antibodies against Giantin (A-R-R#05 Recombinant Antibody Platform Institut Curie, 1:100), GPP130 (a gift from A. Linstedt), OSBP (Atlas Antibodies, HOA039227, lot 000041290, 1:150), TGN46 (Bio-Rad, catalog no. AHP500GT, 1:200), Transferin Receptor (Invitrogen, catalog no. 13-6800, lot UF287715, 1:250), washed three times with PBS and incubated in blocking buffer for 45 min with fluorescently labeled secondary antibodies at 1:400 (Thermo Fisher: Goat anti-rabbit-488 no. A-11008, goat antimouse-488 no. A11001, goat antimouse-568 no. A-11031, donkey anti-sheep-647 A-21448). Nuclei were labeled for 5 min with 5 µg ml^{-1} 4′6-diamidino-2-phenylindole (Vector Laboratories), and mounted using Mowiol (Sigma-Aldrich).

Image acquisition. For analysis of Shiga toxin trafficking shown in Fig. 5d, images were acquired on an inverted Eclipse Ti-E (Nikon) microscope equipped with a spinning disk CSU-X1 (Yokogawa) module, a ×60 CFI Plan Apo VC oil objective and Metamorph software v.1 by Gataca Systems. *Z* stacks were acquired in a step size of 0.4 µm. The pixel size was 0.267 µm. For images shown in Fig. 5a, images were acquired on an SP5 scanning confocal (Leica) with ×63/1.4 Plan Apo oil objective (Zeiss) with pixel size of 0.161 µm and step size of 0.462 µm.

Image analysis. *STxB trafficking*. STxB trafficking was previously characterized[59] by quantification of STxB arrival at Golgi (Giantin), or localization to early endosomes (TfR). Based on this, STxB spots were counted in one central *Z* slice per cell, correlating low numbers to STxB arrival at the Golgi, and high numbers correlating to the cytosolic spots that represent colocalization to early endosomes. Fluorescence area was measured in parallel and remained unchanged in all samples. Data are presented as number of STxB spots normalized to area of fluorescence.

Semiautomated quantification. Fiji ImageJ2 software (National Institutes of Health)[60] was used for image processing and quantification. Quantification was semiautomated by applying Max Entropy automatic threshold to individual cells to determine areas of positive fluorescence (for STxB or TGN46), then counting the number of fragments above threshold per cell by using the 'analyze particles' command.

OSBP relocalization. The integrated density of OSBP was measured in the Golgi region of interest (ROI) (TGN46 from the step above), then normalized to the integrated density for OSBP in whole cell ROI.

Statistics for image analysis. Statistics were performed in GraphPad PRISM10 software. Where data were not normally distributed (Golgi fragmentation and OSBP localization), data were transformed (log$_{10}$) to normalize distribution before performing one-way analysis of variance (ANOVA), with Dunnett's multiple comparisons test to compare each treatment group to control. Graphs show nontransformed data. A *P* value of 0.05 or less was considered significant. The number of cells from independent experiments quantified is detailed in the figure legends.

Protein synthesis assays in cells exposed to Shiga toxins. HeLa cells were grown at 37 °C in an atmosphere of 5% CO$_2$ and 95% air on 150 cm^2 tissue culture flasks in DMEM (Invitrogen) containing 10% SVF, 2 mM L-glutamine, 0.1 mM nonessential amino acids, 100 U ml^{-1} penicillin and 100 µg ml^{-1} streptomycin. First, the cells were plated at a density of 10,000 cells per well in 96-well Cytostar T scintillating microplates with scintillator incorporated into the polystyrene plastic (100 µl per well). Then, complete DMEM medium supplemented with compound was added (50 µl per well). After a short incubation time, complete DMEM medium supplemented with Stx1 (List Laboratory) was added to each well of HeLa-seeded scintillating microplates (dilutions of Stx1 ranging from 10^{-9} to 10^{-16} M; 50 µl per well). After incubation for 20 h, the media (200 µl per well) were removed and replaced with DMEM without leucine containing 10% SVF, 2 mM L-glutamine, 0.1 mM nonessential amino acids, 1% penicillin–streptomycin supplemented by 0.5 µCi ml^{-1} [^{14}C]-leucine. The cells were grown for an additional 5 h at 37 °C in an atmosphere of 5% CO_2 and 95% air. Protein biosynthesis was determined by measuring the incorporation of radiolabeled leucine using a Wallac MicroBeta Trilux scintillation counter[61].

The mean percentage of protein biosynthesis was determined and normalized from duplicate wells. All values are expressed as means ± s.d. Data were fitted with Prism v.5 software (Graphpad Inc.) to obtain the 50% effective toxin concentration (EC_{50}). Plotting $(1 - EC_{50}) \times 100/(1 - EC_{50\mathrm{max}})$ as a function of compound concentration enables the calculation of the IC_{50}, which represents the concentration of compound giving 50% of its inhibitory effect. The goodness of fit for each toxin and drug was assessed by R^2 and confidence intervals.

Molecular modeling. For this, the software packages used were Maestro v.13.3.121 and MMshare v.5.9.121, Release 2022-3, on the Windows-x64 platform.

Crystal structure PDB source files were obtained from the PDB (ID 7V62). Protein preparation was carried out using the default workflow with a few minor adjustments. Namely, in the Preprocess workflow, disulfide bonds were created, missing loops (using Prime) were filled in and selected, and the variation of het states was set (using Epik) to a pH range of 7.5 ± 0.5. For the H-bond assignments workflow, H-bonds were assigned using PROPKA at pH 7.5. In the final Minimize and Delete waters workflow, a restrained minimization was performed with a convergence of 0.3 Å to heavy atoms. If water molecules existed in the binding site, the preparation was optimized by running a validation test on the binding of the cognate ligands. Ligand preparation was carried out on all possible stereoisomeric forms of the ligand, which were desalted and ionized at pH 7.5 ± 0.5 using Epik. The force field used was OPLS4.

For initial screenings of crystal structures with ligands, receptor grid generation was carried out centroid on the cocrystallized ligand. High-throughput ligand docking was carried out using Glide, using standard precision with flexible ligands. The settings allowed for sampling of nitrogen inversions and ring conformations. Epik state penalties were applied to docking scores. Three poses for each ligand were generated, allowing for more precise accounts of ligand–protein viability. Postdocking minimization and strain correction were also applied to the scoring of each ligand. Pose views were sampled in correlation to the docking scores. For Induced Fit workflows, the binding domain was centroid on the resident ligand. Ligands were free to sample variations in the ring conformation. In Glide docking, the protein preparation constrained refinement was selected, with a maximum of 20 poses generated. Prime refinement was within 5 Å of ligand poses and the Glide redocking is at standard precision. Pose analysis was performed on all examples provided from the simulation. Key considerations were made regarding the retention of any significant position, residue interactions and orientations that were observed as median averages.

Reporting summary

Further information on research design is available in the Nature Portfolio Reporting Summary linked to this article.

Data availability

The data supporting the findings in this study are available within the paper and its supplementary files. Proteomics data can be found in Supplementary Dataset 1. Raw proteomics data on **1**–**8** and $MnCl_2$ was uploaded to MASSIVE, with the accession number MSV000091726. Raw proteomics data on the iTSA of oxybipin-2, and the expression proteomics of 3 and OSW-1 can be found at MSV000093086. Source data are provided with this paper. Any other data can be requested and will be provided by the corresponding author.

References

60. Schindelin, J. et al. Fiji: an open-source platform for biological-image analysis. *Nat. Methods* **9**, 676–682 (2012).
61. Noel, R. et al. *N*-methyldihydroquinazolinone derivatives of Retro-2 with enhanced efficacy against Shiga toxin. *J. Med. Chem.* **56**, 3404–3413 (2013).

Acknowledgements

The Laraia Laboratory was supported by funding from the Novo Nordisk Foundation (grant nos. NNF19OC0055818, NNF19OC0058183, NNF21OC0067188), the Carlsberg Foundation (grant no. CF19-0072) and the Independent Research Fund Denmark (grant nos. 9041-00241B, 9041-00248B). CeMM and the Winter Laboratory are supported by the Austrian Academy of Sciences. The Winter laboratory is further supported by funding from the European Research Council under the European Union's Horizon 2020 research and innovation program (grant agreement no. 851478), as well as by funding from the Austrian Science Fund (FWF, project nos. P32125, P31690 and P7909). A.F. is an F.R.S.-FNRS Chercheur Qualifié. The Forrester laboratory is funded by an Incentive for Scientific Research Grant (grant no. MIS: F.4518.23) from FNRS. We thank the Morph-Im platform and staff at the University of Namur for their microscopy support. The Gillet laboratory was funded by the French National Research Agency (ANR) under contract nos. LeishmaStop ANR-18-CE18-0016-01 and SMERSEC ANR-20-CE18-0016-01, by University Paris Saclay under contract nos. ReCoVEr and PIMVir, and the Joint ministerial program of R&D against CBRNe risks. We thank Ludger Johannes for helpful discussions and providing fluorescently labeled STxB. We also acknowledge the Cell and Tissue Imaging (PICT-IBiSA) and Nikon Imaging Centre, Institut Curie, a member of the French National Research Infrastructure France-BioImaging (grant no. ANR10-INBS-04).

Author contributions

N.H. and L.L. designed the project. N.H. carried out the compound synthesis, proteomics sample preparation and analysis, and cell biological validation of compounds. L.D. expressed and purified recombinant proteins and developed and performed all biophysical assays and cell viability measurements. C.R. designed, supervised, performed and analyzed proteomics experiments and supported cell biological validation. O.R.D. synthesized von Hippel Lindau probes and conducted their biological analysis. L.C. and A.F. performed and analyzed the Golgi integrity and retrograde trafficking experiments. M.C. performed the HiBit CETSA experiments and OSBP overexpression rescue experiments under supervision of G.E.W. H.P.B.-R. performed and analyzed docking experiments and performed FP experiments. M.M. performed the STx1 inhibition experiments under the supervision of J.B. and D.G. J.H. supported recombinant protein expression and synthesis. L.L. supervised the project. N.H., L.D. and L.L. wrote the paper with input from all authors.

Competing interests

G.E.W. is scientific founder and shareholder of Proxygen and Solgate. The Winter laboratory received funding from Pfizer. The other authors declare no competing interests.

Additional information

Extended data is available for this paper at https://doi.org/10.1038/s41589-024-01653-x.

Supplementary information The online version contains supplementary material available at https://doi.org/10.1038/s41589-024-01653-x.

Correspondence and requests for materials should be addressed to Luca Laraia.

Peer review information *Nature Chemical Biology* thanks Minetaro Arita, Markus Schirle and the other, anonymous, reviewer(s) for their contribution to the peer review of this work.

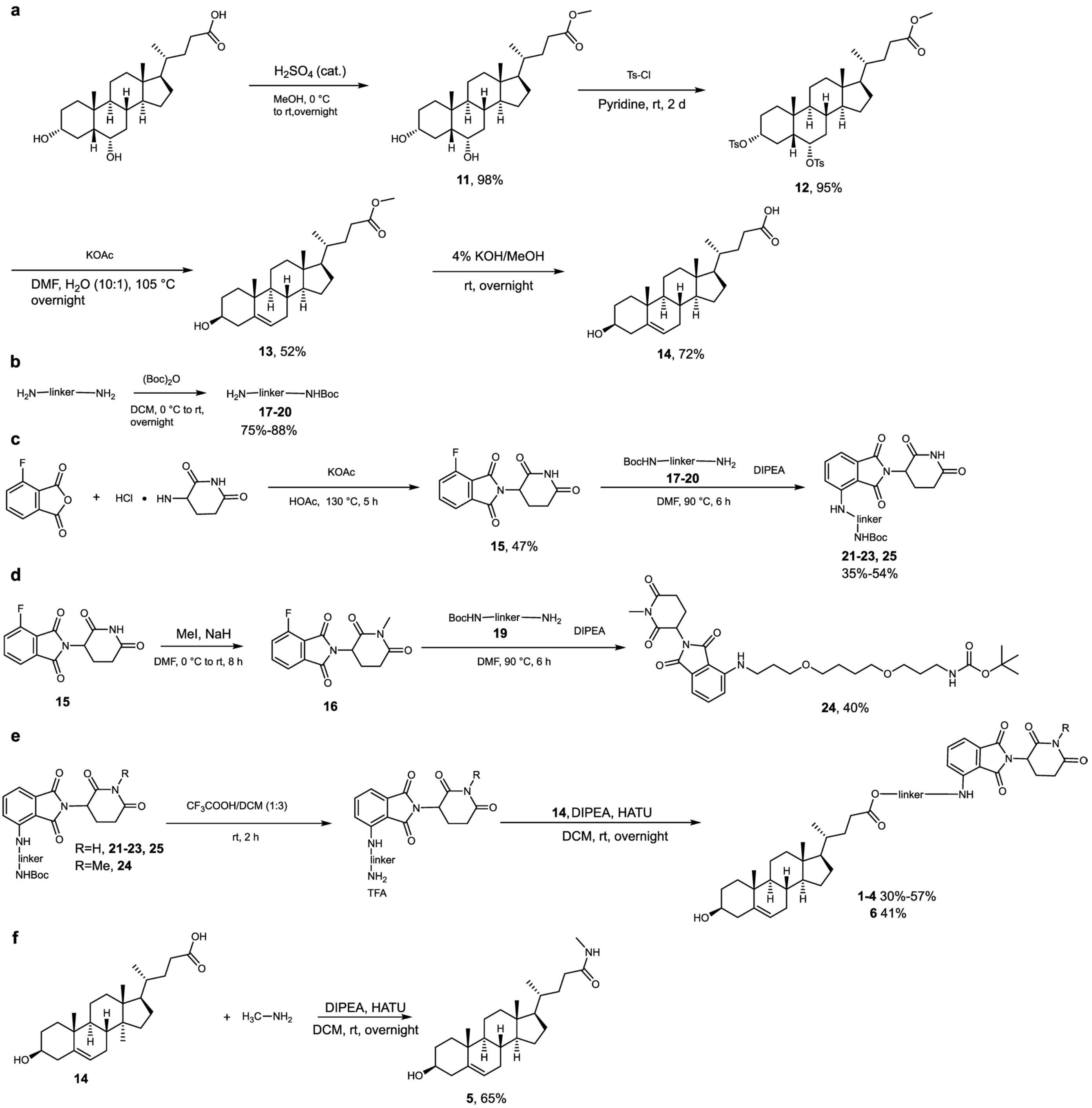

Extended Data Fig. 1 | Synthesis of Cholesterol-bearing bifunctional molecules **1**–**4**, **6** and **5**. (**a**) Synthesis of cholenic acid (14). (**b**) Synthesis of linkers. (**c**) Synthesis of pomalidomide-conjugated linkers. (**d**) Synthesis of methylated negative control precursor (24). (**e**) Synthesis of bichols 1-4 and negative control. (**f**) Synthesis of *N*-methyl cholenamide.

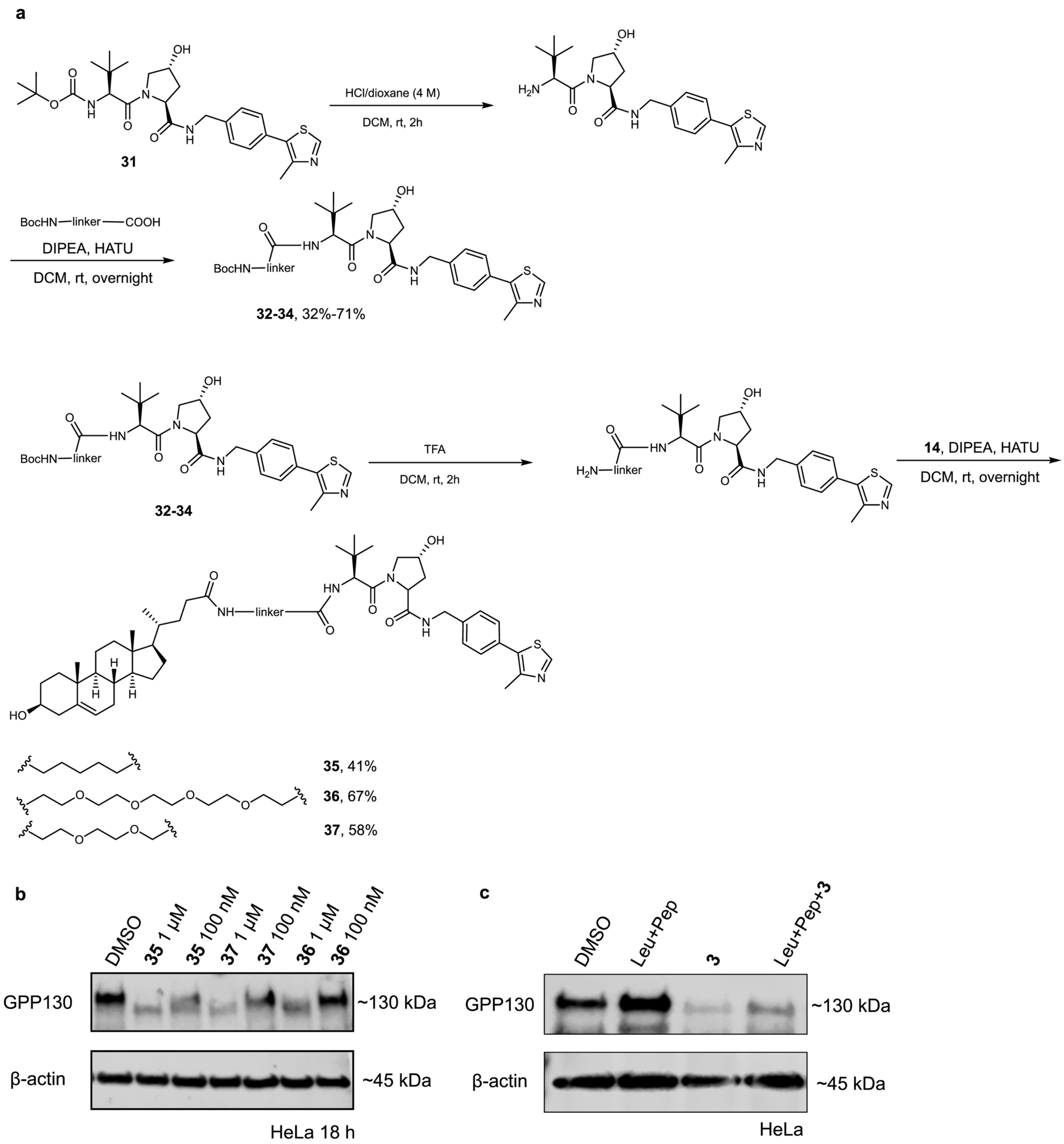

Extended Data Fig. 2 | Degradation of GPP130 by bifunctional molecules containing sterol and vHL recruiting moieties. (**a**) Synthesis of VHL-recruiting PROTACs. (**b**) Effect of VHL-based PROTACs on GPP130 levels in HeLa cells for 18 hours (n = 3, representative experiment shown); (**c**) rescue of GPP130 degradation by lysosomal protease inhibitors Leupeptin (100 µg/mL) and Pepstatin (50 µg/mL); (n=2, representative experiment shown).

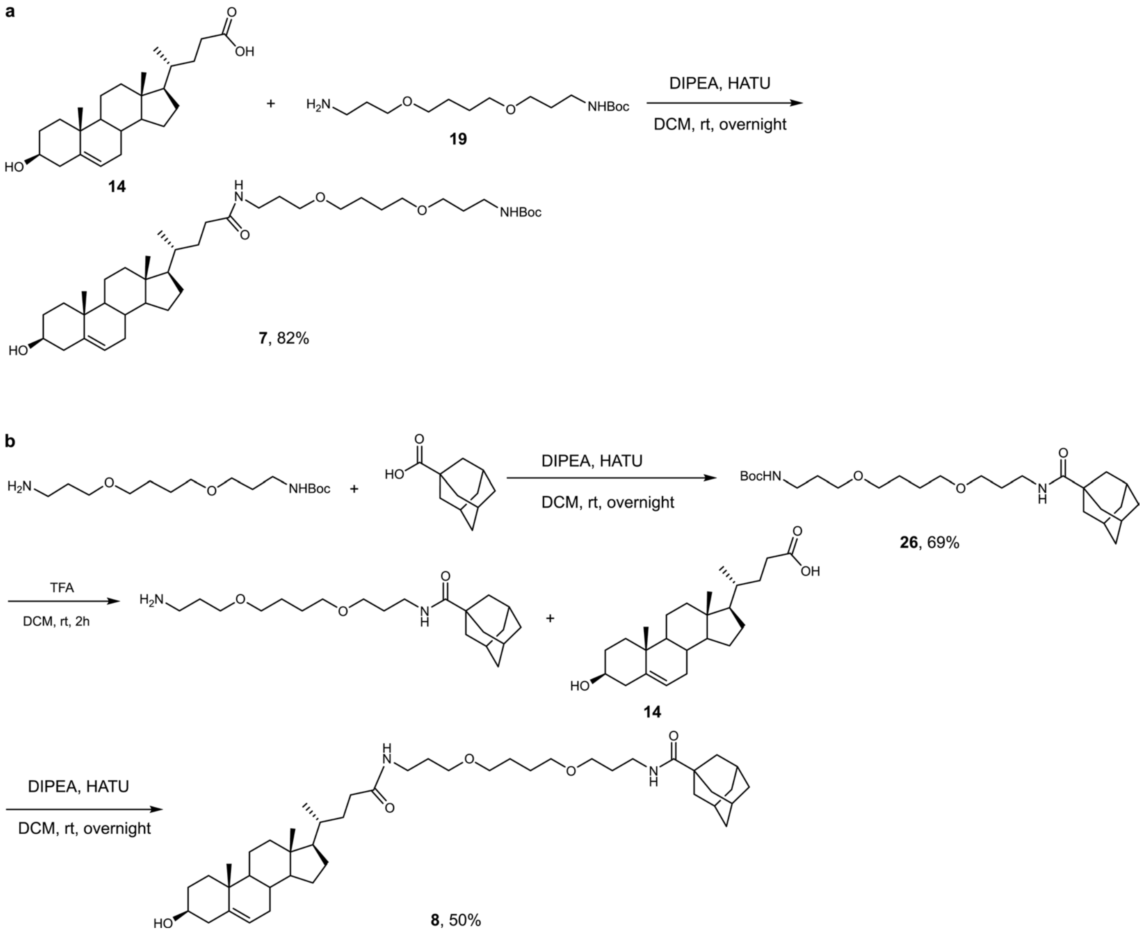

Extended Data Fig. 3 | Synthesis of oxybipins. (**a**) Synthesis of oxybipin-2 (7). (**b**) Synthesis of oxybipin-1 (8).

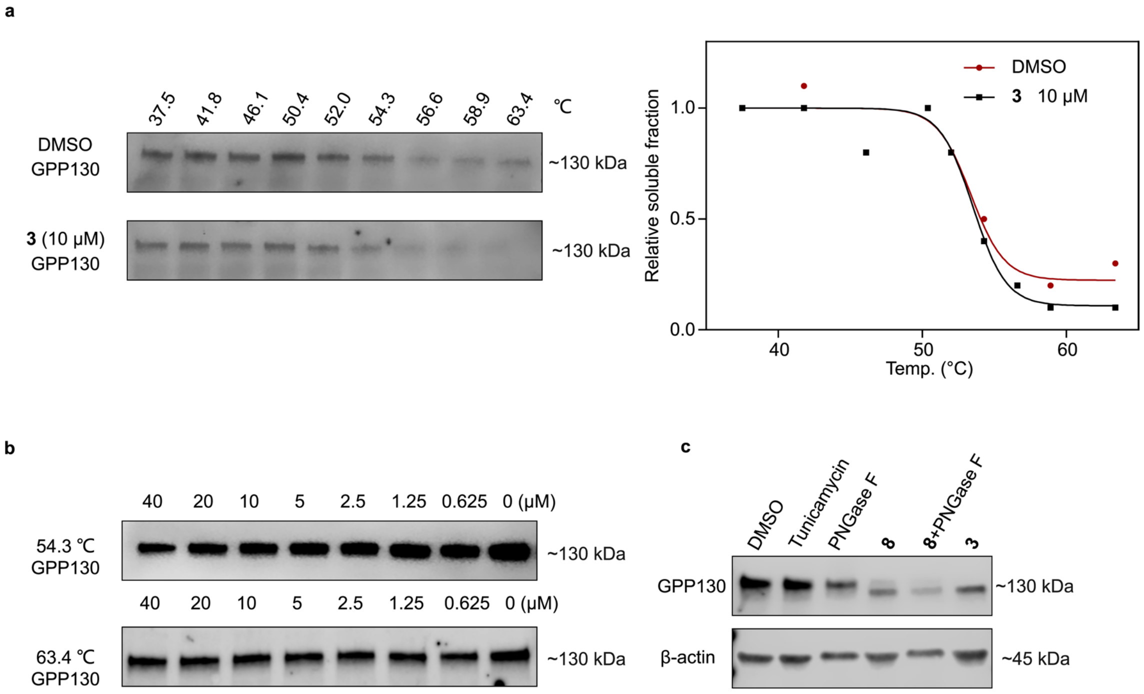

Extended Data Fig. 4 | 3 and its derivatives do not bind to GPP130 directly and do not affect GPP130 *N*-glycosylation. (**a**) Cellular thermal shift assay shows **3** exhibits a weak destabilization effect on GPP130 in intact HeLa cells (n = 2, representative experiment shown). (**b**) Isothermal dose response fingerprinting assay shows **3** failed to destabilize GPP130 in a dose-dependent manner at 54.3 °C (n = 3, representative experiment shown) and 63.4 °C (n = 1) in intact HeLa cells. (**c**) Effect of Tunicamycin (5 μg/mL), PNGase F, **3** and Oxybipin-1 (1 μM each) on the *N*-glycosylation of GPP130 in HeLa cells (n = 2, representative experiment shown).

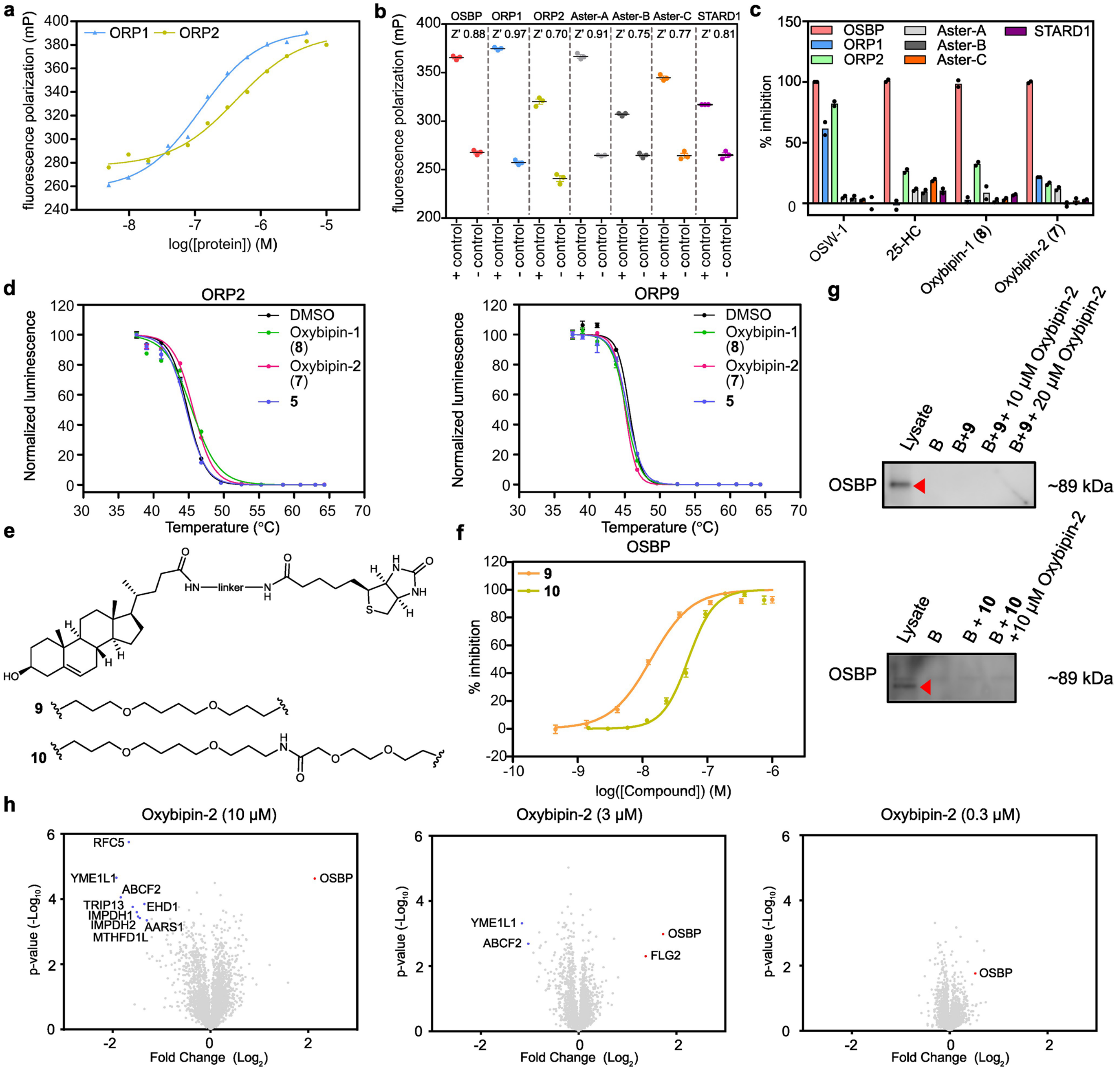

Extended Data Fig. 5 | Oxybipins selectively target OSBP. (**a**) Binding curve of the FP titration of 25-NBD-cholesterol with the ORD of ORP1 and ORP2. Each data point represents the mean of a representative experiment (N=2), from three independent experiments (n=3) (**b**) Calculated Z′ factors using 22-NBD-cholesterol as tracer confirm the robustness of the competitive FP assay selectivity panel. Each data point represents the mean ± s.e.m of three independent experiments (N-2, n=3) (**c**) Screening of **8** (oxybipin-1), **7** (oxybipin-2), OSW-1 and 25-HC in the STP FP selectivity panel at 3 µM, using 22-NBD-Chol as a tracer. Each data point represents the mean of a representative experiment (N=2), from three independent experiments (n=3). (**d**) Effect on the stability of ORP2 and ORP9 by oxybipin-1 and -2 in intact KBM7 cells expressing HiBit tagged fusion proteins. Each data point represents mean ± s.e.m from three technical replicates of a representative experiment, from three independent experiments (N=3, n=3). (**e**) Chemical structures of **9** and **10**. (**f**) Dose-dependent inhibition of GST-OSBP-ORD binding to 22-NBD-Chol by **9** and **10** as assessed by FP. Data are represented as mean ± s.e.m from three independent experiments (N=2, n=3). (**h**) **9** and **10** failed to enrich OSBP in pulldown experiments (n = 1). (**g**) Stabilization profile of oxybipin-2 at 10 µM, 3 µM and 0.3 µM. The destabilized proteins (blue dots) and stabilzed proteins (red dots) were plotted as $\log_2$ fold change (compound-treated /DMSO-treated) versus -$\log_{10}$ (p-value). P-values were determined by a Student's two-tailed *t* test assuming equal variances from the data of three replicates.

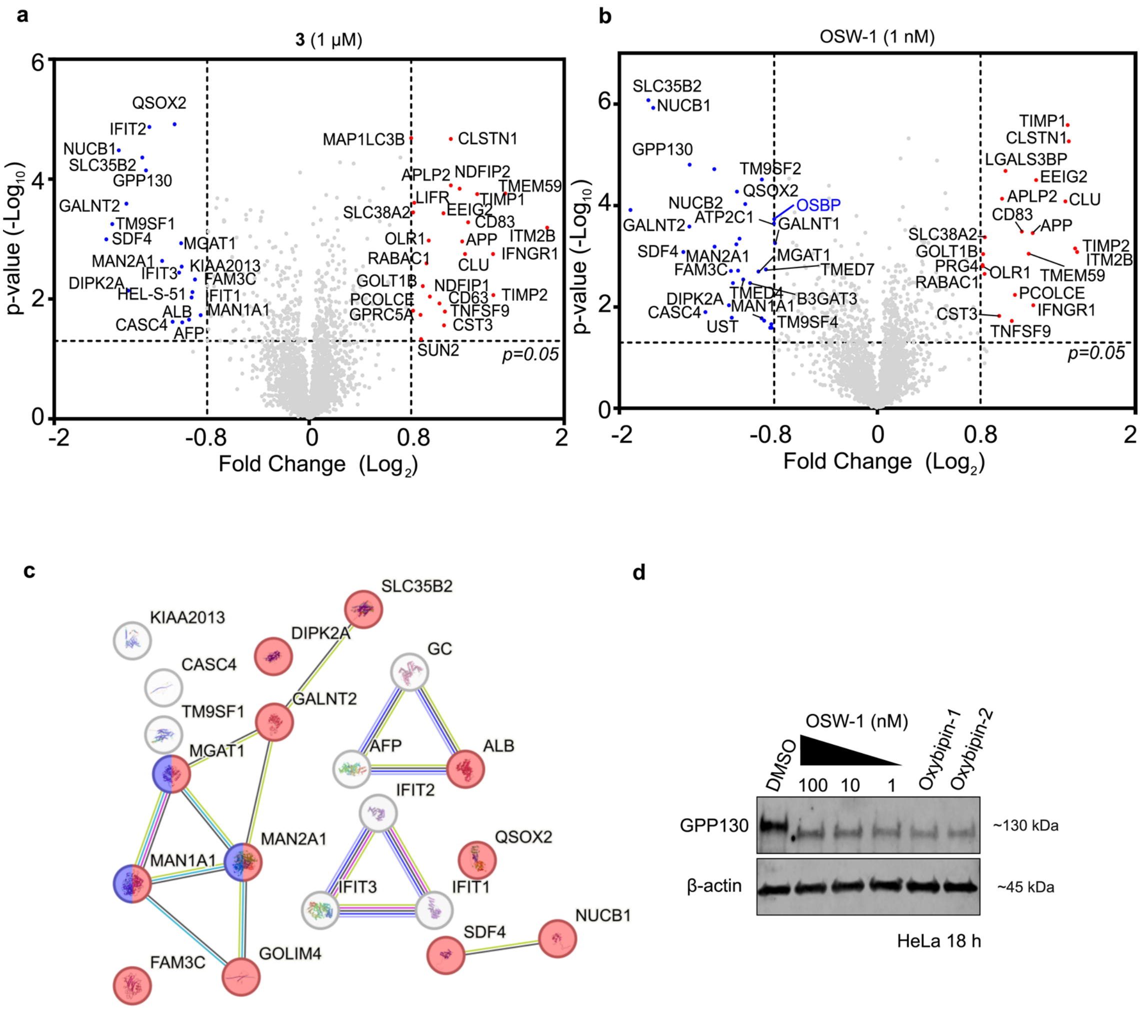

Extended Data Fig. 6 | Expression proteomics of HeLa cells treated with 3 and OSW-1. (**a**) Expression proteomics profile of HeLa cells treated with **3** (1 µM) for 18 h. The down-regulated proteins (blue dots) and up-regulated proteins (red dots) were plotted as log2 fold change (compound-treated / DMSO-treated) versus -log10 (p-value). P-values were determined by a Student's two-tailed *t* test assuming equal variances from the data of three replicates. The dotted horizontal line marks the significance threshold of p = 0.05 and dotted vertical lines represent the threshold of an absolute log2 fold change of 0.8. (**b**) Expression proteomics profile of HeLa cells treated with OSW-1 (1 nM) for 18 hours. (**c**) The down-regulated proteins of **3** can also be classified into Golgi proteins (Red) and proteins involved in *N*-Glycan biosynthesis (Blue). (**d**) Effect of OSW-1 and oxybipins on GPP130 degradation. HeLa cells were treated with indicated concentrations of OSW-1 and 1 µM oxybipins for 18 hours (n = 2, representative experiment shown).

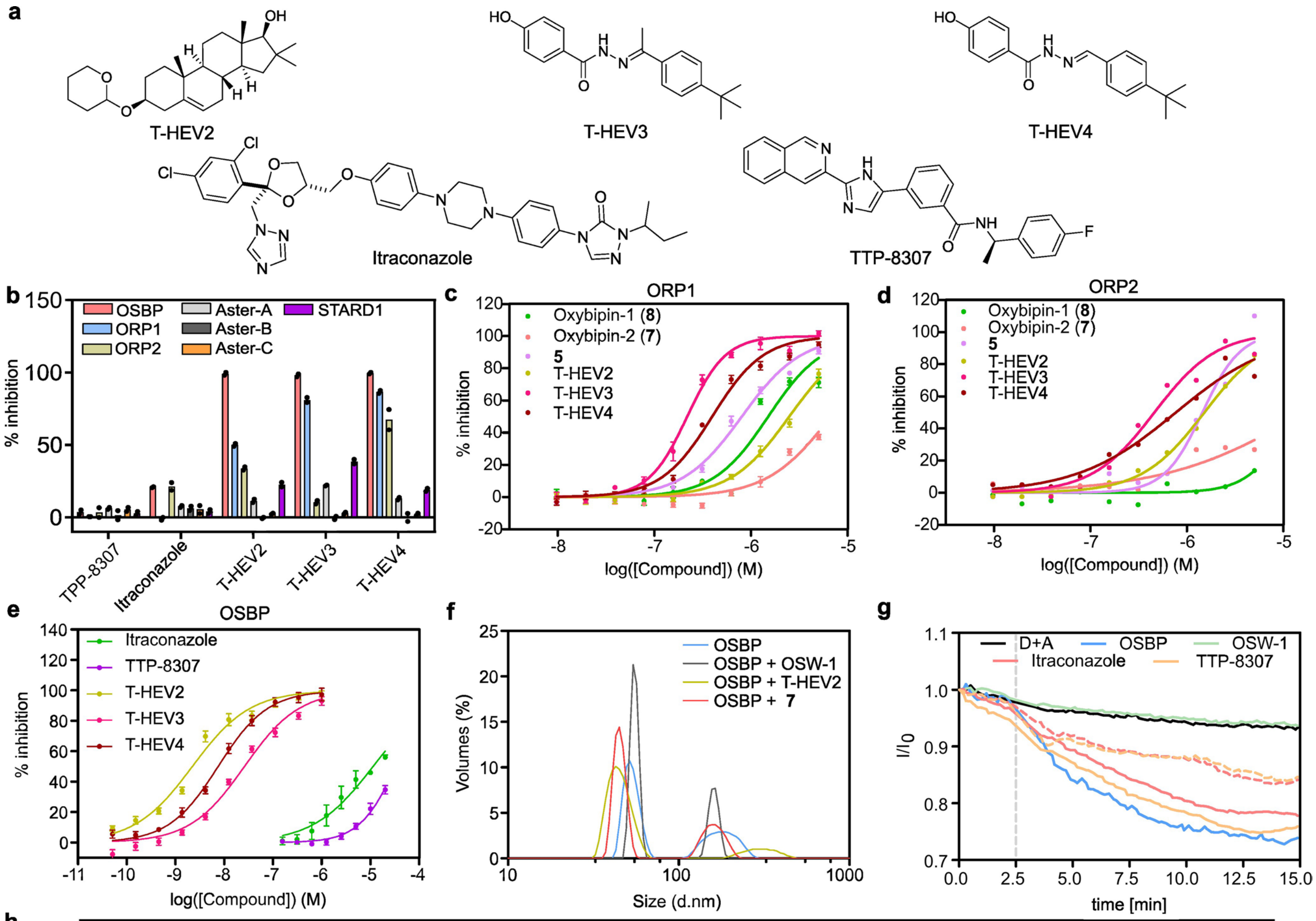

h

	IC$_{50}$ [nM]						
	OSBP	**ORP1**	**ORP2**	**STARD1**	**Aster-A**	**Aster-B**	**Aster-C**
Oxybipin-1	77	1504	>10000	> 10000	> 10000	> 10000	> 10000
Oxybipin-2	13	6686	>10000	> 10000	> 10000	> 10000	> 10000
5	477	803	1450	> 10000	> 10000	> 10000	> 10000
T-HEV2	2	2485	1518	> 10000	> 10000	> 10000	> 10000
T-HEV3	26	219	461	> 10000	> 10000	> 10000	> 10000
T-HEV4	8	396	770	> 10000	> 10000	> 10000	> 10000
Itraconazole	> 10000	> 10000	>10000	> 10000	> 10000	> 10000	> 10000
TPP-8307	> 10000	> 10000	>10000	> 10000	> 10000	> 10000	> 10000

Extended Data Fig. 7 | STP FP selectivity panel reveals lack of selectivity of published OSBP inhibitors. (**a**) Chemical structures of reported OSBP inhibitors T-HEV2, T-HEV3, T-HEV4, Itraconazole and TTP-8307. (**b**) Screening of TTP-8307, Itraconazole, T-HEV2, T-HEV3 and T-HEV4 in the STP FP selectivity panel at 1 µM, with 22-NBD-Chol as a tracer. Each bar represents the mean of a representative experiment, from two independent experiments (N=2, n=2). (**c**) Fluorescence polarization measurements of dose-dependent inhibition of ORP1-ORD binding to 25-NBD-Chol. Data are represented as mean ± s.e.m from three independent experiments (N=2, n=3). (**d**) Fluorescence polarization measurements of dose-dependent inhibition of ORP2-ORD binding to 25-NBD-Chol. Each data point represents the mean of a representative experiment, from three independent experiments (n=3) (**e**) Fluorescence polarization measurements of dose-dependent inhibition of GST-OSBP-ORD binding to 22-NBD-Chol. Data are represented as mean ± s.e.m from three independent experiments (N=2, n=3). (**f**) DLS measurements of GST-OSBP-ORD and GST-OSBP-ORD incubated with different OSBP inhibitors. One representative experiment was shown from three replicates (n=3). (**g**) Inhibition of sterol transport by GST-OSBP(ORD) (500 nM) in liposomes using a FRET assay. OSW-1 was tested at 1 µM, while itraconazole and TTP-8307 were tested at 1 µM (solid lines) and 10 µM (dashed lines). One representative experiment was shown from two independent replicates (n=2). (**h**) IC$_{50}$ values of TTP-8307, Itraconazole, T-HEV2, T-HEV3, T-HEV4, **5**, oxybipin-1 and oxybipin-2 against STPs in FP experiments.

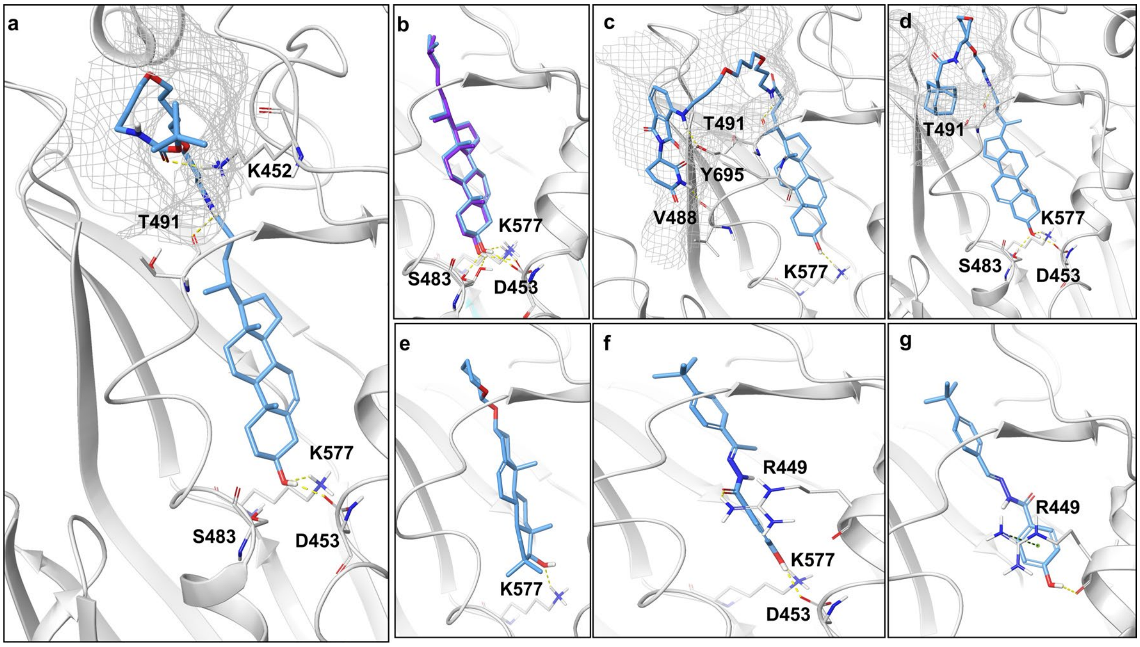

Extended Data Fig. 8 | Predicted binding modes of OSBP inhibitors. Docking poses of oxybipin-2 (**a**), Cholesterol (**b**) (Purple – crystal structure pose, Blue – Docking pose), **3** (**c**), oxybipin-1 (**d**), T-HEV2 (**e**), T-HEV3 (**f**), and T-HEV4 (**g**) into the crystal structure of OSBP's cholesterol binding domain (PDB ID:7V62)[44]. Key binding residues are illustrated. Yellow dashes indicate H-bonds. Green dashes indicate cation-pi interactions. Grey mesh represents the exterior surface of the ORD at a 4 Å distance from the ligand.

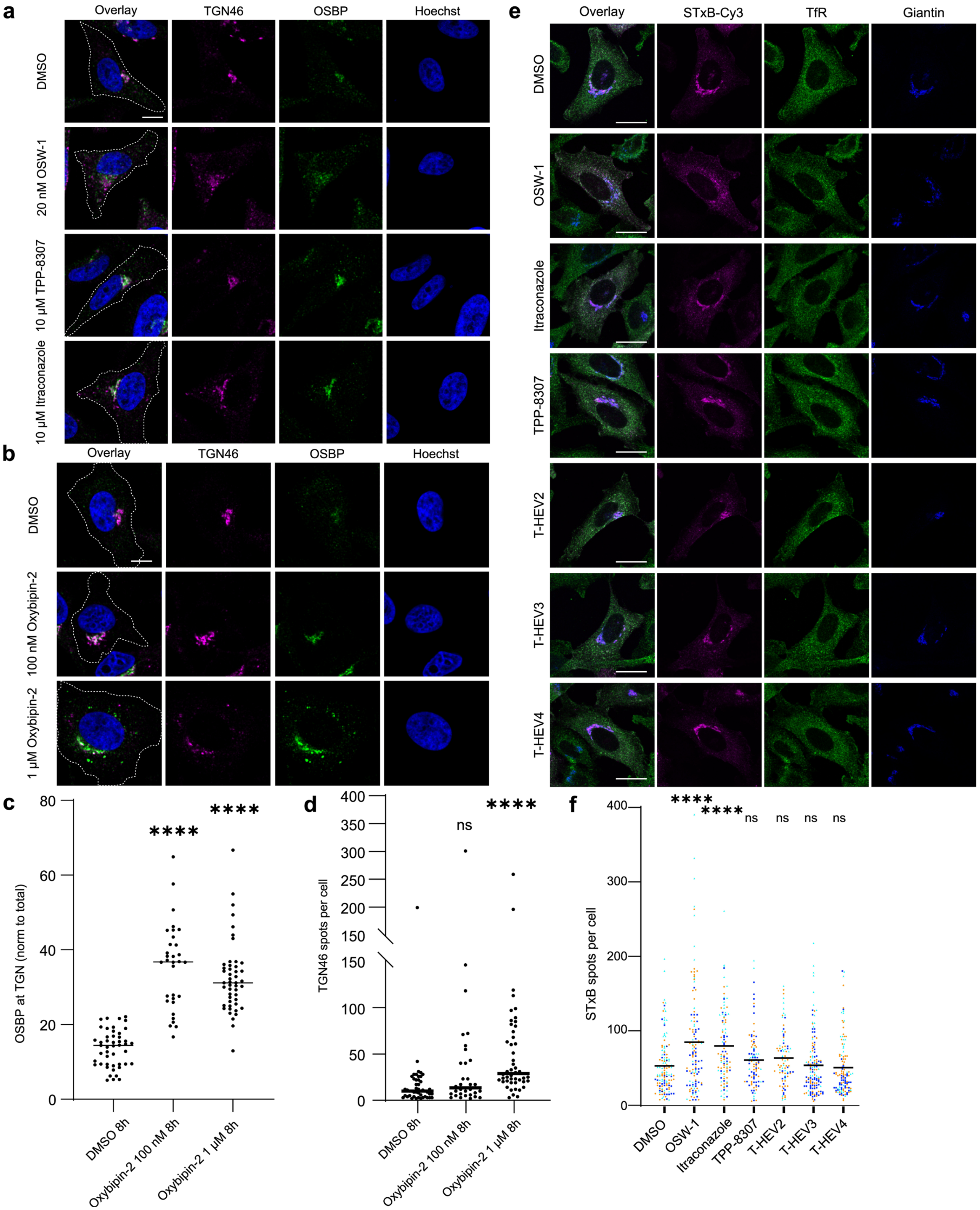

Extended Data Fig. 9 | See next page for caption.

Extended Data Fig. 9 | Effect of OSBP inhibitors on Golgi integrity and OSBP relocalization. (**a**) Scanning confocal microscopy of HeLa cells treated with DMSO, 1 µM Itraconazole or TPP-8307 for 4 h. Cells were immunolabelled with TGN46 (647) and OSBP (488); nuclei labelled with Hoechst. Scale bar = 10 µm, dotted line indicates cell outline. **b**) Scanning confocal microscopy of HeLa cells treated with DMSO, 100 nM or 1 µM oxybipin-2 for 8 h. Cells were immunolabelled with TGN46 (647) and OSBP (488), nuclei labelled with Hoechst. Scale bar = 10 µm, dotted line indicates cell outline. (**c,d**) Graphs show one point per cell, independent experimental replicates (n=3) for a total of 47 (DMSO), 48 (1 µM oxybipin-2), 32 (100 nM oxybipin-2, n=2). **c**) Quantification of OSBP localization to the Golgi, as identified by TGN46. OSBP fluorescence intensity was measured in TGN46 ROI and normalised to total cellular OSBP. One-way ANOVA was performed ($P < 0.0001$) with Dunnett's multiple comparisons test: **** $P < 0.0001$. (**d**) Quantification of TGN46 fragmentation measured by number of spots per cell, line represents median. One-way ANOVA was performed on log10 transformed data ($P < 0.0001$) with Dunnett's multiple comparison test: ns = 0.00828, **** $P < 0.0001$. (**e-f**) STxB trafficking is inhibited by OSBP inhibition but not control compounds. (**e**) Scanning confocal images of STxB-Cy3 trafficking in HeLa cells treated for 4 h with DMSO vehicle, 10 µM Itraconazole, TPP-8307, THEV2, THEV3 or THEV4, or for 2 h with 20 nM OSW1. Cells were immunolabelled with transferrin receptor (TfR, 488), giantin (647) and nuclei stained with Hoechst. Scale bar = 20 µm. (**f**) Quantification of STxB trafficking measured by number of spots per cell. Graph shows one point per cell, shape represents each independent experimental replicate (n=3) for a total of 132 (DMSO), 124 (OSW1), 102 (Itraconazole), 98 (TPP-8307), 91 (THEV2), 141 (THEV3), 124 (THEV4), line indicates mean. One-way ANOVA $P < 0.0001$, Dunnett's multiple comparison test: **** $P < 0.0001$, ns=0.6790 (TPP-8307), ns=0.3904 (THEV2), ns>0.9999 (THEV3), ns=0.9968 (THEV4).

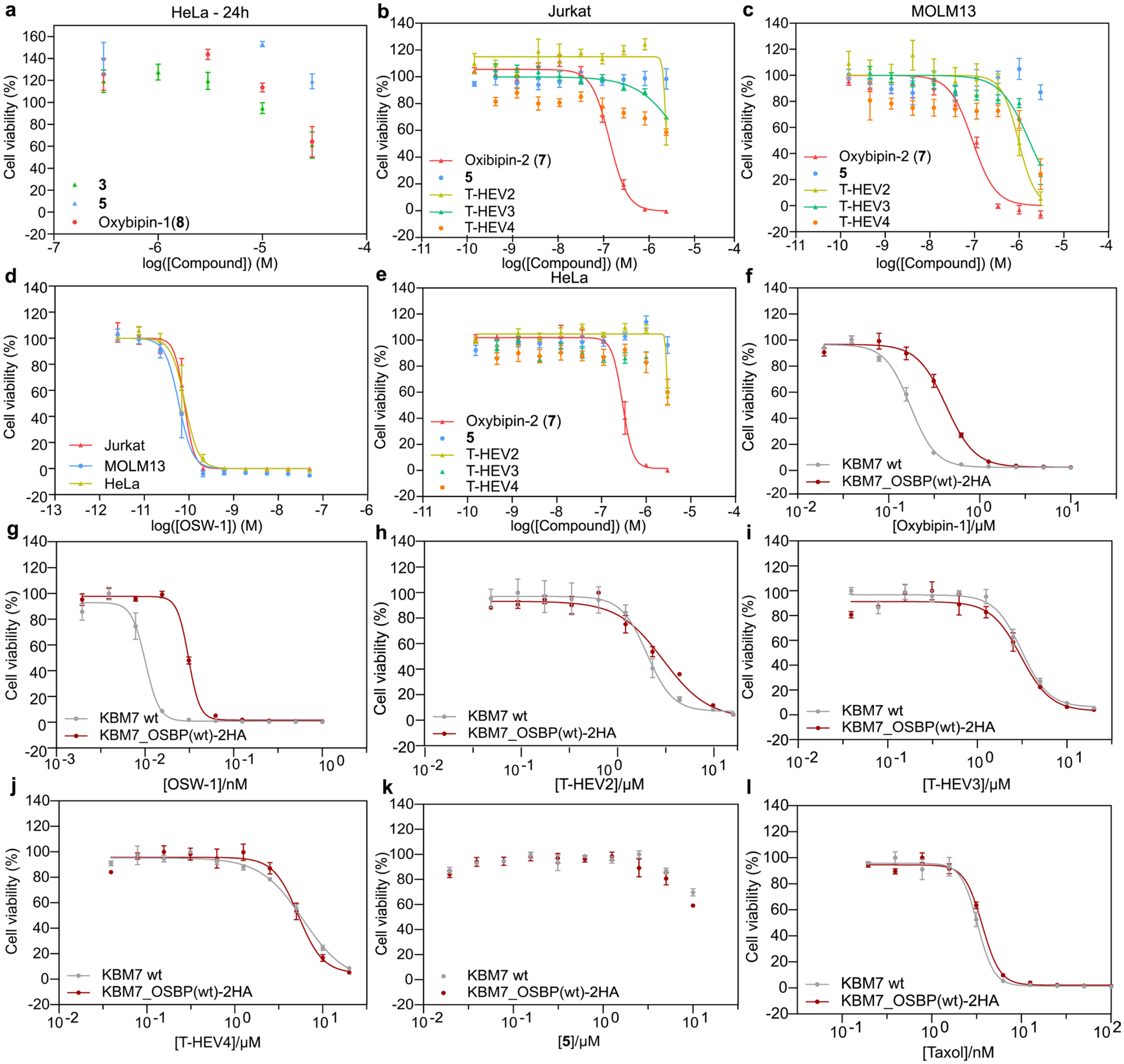

Extended Data Fig. 10 | Effects of oxybipins on cancer cell viability. (**a**) Effect of **3** and oxybipin-1 on HeLa cell viability at 24 h. Each data point represents mean± s.e.m from two technical replicates, two independent experiments. (N=2, n=2) (**b-e**) Effect of oxybipins and control compounds on the viability of cancer cells at 72 h. All data in mean ± s.e.m for three replicates (N=2, n=3). (**f-l**) Effect of oxybipins and control compounds on the viability of KBM7 wildtype cells and KBM7 cells overexpressing OSBP(wt)-2HA at 72 h. Each data point represents mean ± s.e.m from three technical replicates of a representative experiment, from three independent experiments (N=3, n=3).

nature portfolio

Corresponding author(s): Luca Laraia

Last updated by author(s): Apr 29, 2024

Reporting Summary

Nature Portfolio wishes to improve the reproducibility of the work that we publish. This form provides structure for consistency and transparency in reporting. For further information on Nature Portfolio policies, see our Editorial Policies and the Editorial Policy Checklist.

Statistics

For all statistical analyses, confirm that the following items are present in the figure legend, table legend, main text, or Methods section.

n/a	Confirmed	
☐	☒	The exact sample size (*n*) for each experimental group/condition, given as a discrete number and unit of measurement
☐	☒	A statement on whether measurements were taken from distinct samples or whether the same sample was measured repeatedly
☐	☒	The statistical test(s) used AND whether they are one- or two-sided *Only common tests should be described solely by name; describe more complex techniques in the Methods section.*
☒	☐	A description of all covariates tested
☐	☒	A description of any assumptions or corrections, such as tests of normality and adjustment for multiple comparisons
☐	☒	A full description of the statistical parameters including central tendency (e.g. means) or other basic estimates (e.g. regression coefficient) AND variation (e.g. standard deviation) or associated estimates of uncertainty (e.g. confidence intervals)
☐	☒	For null hypothesis testing, the test statistic (e.g. *F*, *t*, *r*) with confidence intervals, effect sizes, degrees of freedom and *P* value noted *Give P values as exact values whenever suitable.*
☐	☒	For Bayesian analysis, information on the choice of priors and Markov chain Monte Carlo settings
☒	☐	For hierarchical and complex designs, identification of the appropriate level for tests and full reporting of outcomes
☒	☐	Estimates of effect sizes (e.g. Cohen's *d*, Pearson's *r*), indicating how they were calculated

Our web collection on statistics for biologists contains articles on many of the points above.

Software and code

Policy information about availability of computer code

Data collection	Li-COR Odyssey Fc was used for WB image acquisition. Immunofluorescence images were acquired on an inverted Eclipse Ti-E (Nikon) microscope equipped with a spinning disk CSU-X1 (Yokogawa) module, a x60 CFI Plan Apo VC oil objective. A Tecan Spark Cyto 600 was used for FP measurements. Luminescence signal was measured on the Multilabel Plate Reader Platform Victor X3 model 2030 (Perkin Elmer). MS data was acquired on a Orbitrap Eclipse™ Tribid™ mass spectrometer (ThermoFisher Scientific).
Data analysis	Graphpad Prism versions 9.5.1, 9. 41, 5.3, 10, were was used for curve-fitting and statistical analysis. MestreNova were used for NMR analysis. Confocal images were analysed using Metamorph software (v1) by Gataca Systems. Fiji ImageJ2 software (National Institute of Health) was used for image processing and quantification. Mass spectrometric raw files were analyzed with MaxQuant (version 1.6.2.10, https://maxquant.org/) and/or proteome discoverer. Modelling was carried out with Maestro version 13.3.121 and MMshare Version 5.9.121.

For manuscripts utilizing custom algorithms or software that are central to the research but not yet described in published literature, software must be made available to editors and reviewers. We strongly encourage code deposition in a community repository (e.g. GitHub). See the Nature Portfolio guidelines for submitting code & software for further information.

Data

Policy information about availability of data

All manuscripts must include a data availability statement. This statement should provide the following information, where applicable:

- Accession codes, unique identifiers, or web links for publicly available datasets
- A description of any restrictions on data availability
- For clinical datasets or third party data, please ensure that the statement adheres to our policy

The authors declare that the data supporting the findings of this study are available within the paper and its supplementary information files. Additional raw proteomics data is available on the MASSIVE server with accession numbers MSV000091726 and MSV000093086.

Human research participants

Policy information about studies involving human research participants and Sex and Gender in Research.

Reporting on sex and gender	n/a
Population characteristics	n/a
Recruitment	n/a
Ethics oversight	n/a

Note that full information on the approval of the study protocol must also be provided in the manuscript.

Field-specific reporting

Please select the one below that is the best fit for your research. If you are not sure, read the appropriate sections before making your selection.

☒ Life sciences ☐ Behavioural & social sciences ☐ Ecological, evolutionary & environmental sciences

For a reference copy of the document with all sections, see nature.com/documents/nr-reporting-summary-flat.pdf

Life sciences study design

All studies must disclose on these points even when the disclosure is negative.

Sample size	All presented data is based on cultured human cell lines. No statistical methods were used to pre-determine sample size. Sample sizes were chosen as at least n = 3 , as these are sufficient to observe variance and trends between groups and to ensure reproducibility between measurements, based on previous work in our group and in the field (e.g. Laraia et al, Nat Chem Biol 2019).
Data exclusions	In quantitative proteomics, only proteins with > 1 peptide and > 1 protein unique peptide detected in all three replicates were considered for downstream analysis.
Replication	All experiments were carried out in at least 3 biological replicates where possible, to ensure that data was consistent between replicates. All replication attempts were successful.
Randomization	When an experiment was commenced, groups of cells were allocated into treatment groups without pattern or bias. This ensured that each treatment group in an experiment were identical (within the inherent variation caused by cell seeding).
Blinding	No experiments performed on experimental groups that would require blinding during allocation were performed. Blinding was not performed during growth curve, biochemical, biophysical, and structural studies described as these methods are not considered to be biased by subjects conducting experiments and are typically performed without blinding.

Reporting for specific materials, systems and methods

We require information from authors about some types of materials, experimental systems and methods used in many studies. Here, indicate whether each material, system or method listed is relevant to your study. If you are not sure if a list item applies to your research, read the appropriate section before selecting a response.

Materials & experimental systems

n/a	Involved in the study
☐	☒ Antibodies
☐	☒ Eukaryotic cell lines
☒	☐ Palaeontology and archaeology
☒	☐ Animals and other organisms
☒	☐ Clinical data
☒	☐ Dual use research of concern

Methods

n/a	Involved in the study
☒	☐ ChIP-seq
☒	☐ Flow cytometry
☒	☐ MRI-based neuroimaging

Antibodies

Antibodies used	GOLIM4 Polyclonal Antibody Invitrogen PA5-51624 1: 1000 Anti-QSOX2 antibody Abcam ab121376 1: 1000 Anti-OSBP antibody produced in rabbit Sigmaaldrich HPA039227 1: 1000 Anti-OSBP2 antibody produced in rabbit Sigmaaldrich HPA021514 1: 1000 Beta Actin Monoclonal Antibody (AC-15) Invitrogen AM4302 1: 5000 Goat anti-Rabbit IgG (H+L) Secondary Antibody, HRP Invitrogen 31460 1: 10,000 F(ab')2-Goat anti-Mouse IgG (H+L) Secondary Antibody, HRP Invitrogen A24512 1: 10,000 IRDye® 800CW Goat anti-Mouse IgG (H + L) LI-COR 925-32210 1: 15,000 IRDye® 680RD Goat anti-Rabbit IgG (H + L) LI-COR 925-68071 1: 15,000 Donkey anti-Sheep IgG (H+L) Cross-Adsorbed Secondary Antibody, Alexa Fluor™ 647, Invitrogen A-21448 Sheep anti Human TGN46, Biorad, AHP500GT, 1:200 Transferrin Receptor Monoclonal Antibody (H68.4), Invitrogen, 13-6800
Validation	Antibodies were validated by the suppliers as follows: GOLIM4 Polyclonal Antibody Rabbit GOLIM4 antibody was verified by Relative expression to ensure that the antibody binds to the antigen stated. Application: IHC, ICC/IF Anti-QSOX2 antibody Rabbit Polyclonal QSOX2 antibody. Suitable for IHC-P, WB, ICC/IF and reacts with Human samples. Anti-OSBP antibody produced in rabbit Anti-OSBP antibody produced in rabbit Prestige Antibodies® Powered by Atlas Antibodies, affinity isolated antibody, buffered aqueous glycerol solution. All Prestige Antibodies Powered by Atlas Antibodies are developed and validated by the Human Protein Atlas (HPA) project and as a result, are supported by the most extensive characterization in the industry. Anti-OSBP2 antibody produced in rabbit Anti-OSBP2 antibody produced in rabbit Prestige Antibodies® Powered by Atlas Antibodies, affinity isolated antibody, buffered aqueous glycerol solution. All Prestige Antibodies Powered by Atlas Antibodies are developed and validated by the Human Protein Atlas (HPA) project and as a result, are supported by the most extensive characterization in the industry. Beta Actin Monoclonal (AC-15) Antibody Mouse Beta Actin antibody was verified by knockdown to ensure that the antibody binds to the antigen stated. Application: WB, IHC, ICC/IF, Flow, Misc Sheep anti Human TGN46 This product has been reported to work in the following applications. This information is derived from testing within our laboratories, peer-reviewed publications or personal communications from the originators. Application: WB, IHC, IF, IP, ELISA, etc. Transferrin Receptor Monoclonal Antibody (H68.4) Mouse Transferrin Receptor antibody was verified by Knockdown to ensure that the antibody binds to the antigen stated. Application: WB, IHC, ICC/IF, Flow, ELISA, IP, in situ PLA, etc.

Eukaryotic cell lines

Policy information about cell lines and Sex and Gender in Research

Cell line source(s)	HeLa (ATCC), A549 (ATCC), Jurkat (ATCC), MOLM13 (DSMZ), KBM7 (Brummelkamp Lab)
Authentication	Cell lines were authenticated by suppliers. https://www.atcc.org/products/ccl-2 and https://www.atcc.org/products/ccl-185 and https://www.atcc.org/products/tib-152 and https://www.dsmz.de/collection/catalogue/details/culture/ACC-554 The KBM7 cell line (Carette et al, Science, 2009) was authenticated using short tandem repeat profiling.
Mycoplasma contamination	All cell lines tested negative for Mycoplasma contamination.
Commonly misidentified lines (See ICLAC register)	To the best of our knowledge we did not use commonly misidentified cell lines